Bundesamt
für Strahlenschutz

Ressortforschungsberichte zum Strahlenschutz

Modellierung von Hydrodynamik und Stofftransport bei wassergebundenen Transportprozessen im Strahlenschutz unter Berücksichtigung der Freigabe schwach radioaktiver Stoffe

Vorhaben 3618E03510

Universität Stuttgart

R. Winter
Prof. Dr. B. Flemisch
Prof. Dr. H. Class

Das Vorhaben wurde mit Mitteln des Bundesministeriums für Umwelt, Naturschutz, nukleare Sicherheit und Verbraucherschutz (BMUV) und im Auftrag des Bundesamtes für Strahlenschutz (BfS) durchgeführt.

Impressum

Bundesamt für Strahlenschutz
Postfach 10 01 49
38201 Salzgitter

Tel.: +49 30 18333-0
Fax: +49 30 18333-1885
E-Mail: ePost@bfs.de
De-Mail: epost@bfs.de-mail.de

www.bfs.de

BfS-RESFOR-219/24

Bitte beziehen Sie sich beim Zitieren dieses Dokumentes immer auf folgende URN: urn:nbn:de:0221-2024032642449

Salzgitter, März 2024

Content

1 Introduction

Classification of this report's subjects The development and extensive use of nuclear power has created an immense challenge worldwide in the handling of radioactive materials. Enormous volumes of radioactive waste have been produced and disposal technologies are developed. While the safe disposal or recycling of high-level radioactive waste seems to remain an unresolved problem for the foreseeable future, intermediate or low-level waste may undergo less severe restrictions in its treatment if the relevant conditions are met. In this context, the term clearance refers to the situation that levels of radionuclides in a material are so small that the material can be released from regulatory control. In order to determine these levels, it is required to predict the transport of radionuclides with appropriate mathematical/numerical tools.

A major conceptual issue arises in how radionuclides are considered in transport models. They may be viewed as solutes with or without coupling to fluid properties like density and viscosity, or they may be occurring with colloidal particles, which is conceptually much more complex and associated with a demand for additional specific data. A major difference between solute transport and colloid transport is due to the fact that fluid velocities are representative for solute transport, while colloids can have their own dynamics dependent on their density relative to the fluid density, the orientation of the flow, the hydro-geochemistry between rock, colloid particles, and radionuclides, as well as the flow field, i.e. whether it is a homogeneous or heterogeneous flow field such as in rough fractures or in macropores.

Both in the deep subsurface and in the case of landfills as in this report, the flow field itself can already reveal a great variety of hydraulic regimes, which require the flow model to be specifically adapted. In the deep subsurface and in the context of radioactive waste disposal, it is typically the phenomenon of fracture-matrix flow, e.g. in clay or granite host rock, which introduces additional complexity; in landfills, however, one may be confronted with strong heterogeneity or with macropores. The deviation from small Reynolds numbers can lead to non-validity of Darcy's law, which is why more sophisticated approaches need to be considered, typically going along with increased computational effort, more parameters that need to be determined, and with additional conceptual complexity. This will be among the important focal points of this project report.

The definition of appropriate scenarios in terms of boundary conditions for a landfill scenario with radionuclide transport is another important subject of this report. Water-based transport essentially is associated with precipitation events. Questions in this regard comprise the relevant definition of rain events, the quantification of surface discharge, evaporation, and remaining subsurface infiltration rates, all of which may be affected by climate change. Therefore, the definition of scenarios requires hydrological models and the quantitative assessment of their corresponding assumptions on water pathways relevant for clearance.

This project report summarizes the results achieved within the project 'Radiomod', funded by BfS under grant number 3618E03510. At the time of submission of the proposal for this project, its content was very much characterized by the fact that the need for scientific follow-up work was derived from the publication of (Merk, 2012). This publication compared a simplified model, suggested by the International Atomic Energy Agency (IAEA) in their safety report SR 44 (IAEA, 2005), with a more sophisticated simulation model based on the essential physical processes. This report addresses investigations that use conceptual approaches which reach in certain aspects beyond the capabilities of the model used by Merk. On the other hand, Merk's work is used as a reference to test and compare the implementations, which for this particular study were done in the open-source simulator DuMu^x (Koch, et al., 2021).

The 'products' of this work are the scientific insights as reported below as well as a freely available DuMu^x simulation model, which can be used to reproduce the simulation data of this report and to produce further simulation results as required in extended scenarios.

Remark on the Covid19 pandemic The project work was almost in its entire duration affected by the Covid19 pandemic. Planned exchange with the BfS was accordingly strongly delayed, although virtual meetings were held on a regular basis. Access to site-specific data or experimental data, e.g. on sorption or colloids, as originally planned in joint meetings with the BfS could not be realized in the end due to the pandemic situation.

1.1 Task Description

The project work plan included four work packages, which can be briefly summarized as follows:

- **WP1** Different approaches to modelling the hydrodynamics in heterogeneous porous media, also under consideration of partially saturated media, were investigated. This included the Richards equation, which assumes an infinitely mobile gas phase, in comparison with the two-phase flow equations in porous media; furthermore, the comparison of Darcy regimes with Darcy-Forchheimer, the latter can account for potentially relevant inertial effects; also, the flow through potentially occurring macro-pores. This is mainly addressed in Ch. 2 without major deviations from the original work plan.
- **WP2** The transport of radionuclides was coupled to the flow. For this work package, it was planned to enhance the transport model in the DuMu^x simulator with processes related to radionuclides. The enhanced transport model was implemented and can be flexibly coupled to the flow models (see WP1). This work package is mainly reported in Ch. 2.
- **WP3** The implemented model requires validation and verification as well as analysis of uncertainties. The work plan specified a validation by comparing to experimental data, which would be provided by the BfS or other external partners. Mainly due to the Covid19 pandemic, this experimental validation could not be accomplished in cooperation with the BfS. Instead, the model was compared to the Merk model (Merk, 2012), which served as a reference for performing a 3D landfill scenario as it is elaborated on in Ch. 4. In this section, an emphasis is also put on the options to describe the boundary conditions for precipitation events and their impact on the transport of radionuclides.
- **WP4** The relation of the further developed model to the recommendations of the IAEA safety report SR 44 is addressed with some summarizing thoughts and outlooks on further research in the last Chapter of this report.

1.2 Prerequisites of the Project

The project is based on work related to numerical modelling and numerical simulation. As mentioned in the introductory comments above, the prerequisites of the project are given in the SR 44 (IAEA, 2005), the (Merk, 2012) publication and related reports by GRS (Gesellschaft für Anlagen- und Reaktorsicherheit). The literature on radionuclide transport in the subsurface is described below with the scientific and technical state. The tools to further develop and apply the modelling work were available at the University of Stuttgart in form of the numerical simulator DuMu^x. No further prerequisites were necessary.

1.3. Planning and Procedure

Project planning and procedure were outlined in the project proposal. This included comparative studies for flow and transport mechanisms in a landfill, taking into focus the water pathway of potential radionuclides.

It was planned to firstly adapt the numerical simulator DuMu^x to be capable of modelling coupled flow and transport of radionuclides. In parallel, numerical studies were carried out, where the Forchheimer approach was tested and compared to a Darcy approach to find out under which circumstances inertial forces play a potential role. Then we compared the DuMu^x 1D results to (Merk, 2012). The 'best-fit' version of our 1D results in comparison to (Merk, 2012) was used as a reference to extend the model to three dimensions. Concentration breakthrough curves at a virtual measurement point downstream of the landfill proved plausible quantitative agreement between 1D and 3D results, while details will be discussed in the report.

The originally discussed options to consider Brinkman's approach and colloidal transport of radionuclides could unfortunately not be realized. With respect to colloid-based transport, the challenges deemed too big to address this appropriately with the given amount of time, in particular without access to specific data on the realistic occurrence and morphology of macropores, the hydrogeochemical data, and the nature, texture, shape, etc. of potential colloid particles. Concerning Brinkman's approach, the expected amount of time for implementing the, particularly for two-phase flow, complex model, could finally not be allocated within the overall time budget of the project. It was decided to resort only to the already implemented Forchheimer model for the description of flow in macropores.

Additional in-depth results and further analyses are also expected in the doctoral thesis of Roman Winter, which is not completed at the time of writing up this report. This includes in particular a more comprehensive analysis of sensitivities due to the expected realistic ranges of the different model input parameters.

As already mentioned, the Covid19 pandemic has prevented a more intense exchange with Dr. Merk and colleagues from BfS in Munich, which importantly affected any work on validation of the model with experimental data, as it was planned in the original project proposal.

1.4 Scientific and Technical State

As elaborated above, the clearance of contaminated material dumped on a landfill, is so far regulated based on recommendations as given by (IAEA, 2004), (IAEA, 2005) and national specifications, which are in Germany under the responsibility of the German Federal Office for Radiation Protection (BfS). For the specific scenarios to be investigated in this study, the primary scientific reference is the paper by (Merk, 2012).

The SR 44 report describes several scenarios, one of them being concerned with the presence of contaminated material, say on a landfill, which may lead to a release of radionuclides into a groundwater aquifer. This contamination may affect drinking water wells further downstream, and eventually lead to the ingestion of contaminated water or food if the water is used for irrigation.

It is further important to mention work carried out by the GRS (Gesellschaft für Anlagen- und Reaktorsicherheit) in the field of clearance, in particular the report of (Artmann, et al., 2014) on application and further developments of modelling tools, as well as the related publication of (Seher, et al., 2016).

Review of literature relevant for the project The physical processes of relevance for this project are related to the flow of water through unsaturated and saturated, strongly heterogeneous porous media. This water flow is coupled to the transport of radionuclides, which implies a large variety of transport phenomena, such as advection, diffusion, dispersion, sorption or retardation due to different other effects as, for example, in colloid transport. Since the focus of the project is on numerical modelling, the field of research is also extended on numerical solution schemes, which is related to coupling approaches between flow and transport or efficient solution algorithms and discretization methods.

The literature in this broad field is, accordingly, abundant. In the following, we give a brief exemplary overview of papers, books, and reports, which are of relevance for the topics addressed in this project to reflect the current scientific and technical state.

Fundamentally, this project deals with the clearance, i.e., the evaluation of situations such that sites can be released from regulatory control. As mentioned before, the basic definition of the term 'clearance' is given by the International Atomic Energy Agency in its report on the application of the concepts of exclusion, exemption and clearance (IAEA, 2004). With respect to clearance, already above-mentioned studies in the immediate context of this project are provided by the GRS (Artmann, et al., 2020), (Seher, et al., 2016). Other related literature on clearance scenarios is, for example, found in (Novak, et al., 2014) with references to specific clearance scenarios and 3D simulations of doses, or in (Nagasaki, et

al., 2015), where clearance is put into the general context of radioactive waste engineering and management.

In this particular project, the water pathway is investigated, which implies the flow of water through subsurface compartments where the flow regimes may exhibit different characteristics to be considered appropriately.

Modelling porous-media flow is in fact an old and established discipline and is traditionally traced back to (Darcy, 1856), who stated the linear dependence of flow rates in porous media from an acting pressure gradient. It is, of course, important to emphasize that this holds only if Reynolds numbers are small enough, which will be one of the topics addressed prominently later on in this present project report. Since we have to consider flow through unsaturated media (or: the vadose zone), the presence and potentially the flow of a gas phase need to be considered. A concept for multiphase flow in porous media was proposed by (Buckingham, 1907), where the permeability for the water depends on the content (or: saturation) of water. This concept was extended by (Richards, 1931), who formulated a partial differential equation for unsaturated water flow, which is commonly referred to as the 'Richards equation'. A model that solves the Richards equation was also the basis of the (Merk, 2012) study and is established in simulators, among which maybe the most well- known is HYDRUS (Šimůnek, et al., 2016). A further very fundamental early work is found in (Leverett, 1941) who explains the effects of capillarity in porous solids, which is today established in a variety of parameterizations of the capillary pressure-saturation relationship; the most prominent and well-known approaches are given by (Brooks, et al., 1964) and by (Van Genuchten, 1980)

The books of (Bear, 1972) and (Bear, et al., 1990) are among the most well-known textbooks to provide a comprehensive introduction into the physical processes in porous media flow and transport and their mathematical modelling.

With respect to dispersion processes, which are definitely of high relevance in the transport of radionuclides, it was (Scheidegger, 1961) who proposed a theory which is still commonly acknowledged and corresponding approaches to model dispersion are in use.

A comprehensive overview of numerical methods and discretization schemes for multiphase porous-media flow models is given by (Helmig, 1997). In particular in transport modelling, which is in the case of this project strongly linked to radionuclides and their decay, it is often not appropriate to solve all equations monolithically. Instead, coupling approaches are required, which are exemplarily discussed (Helmig, et al., 2013). The coupling issue and the modelling of transport phenomena are also important in reactive transport modelling and, for example, addressed in the review paper by (Steefel, et al., 2015). More specifically for numerical methods to model radionuclide transport, there are, for example, studies that introduce efficient solution strategies, like the IMPEC method, which solves the pressure equation implicitly and the equation for the concentrations sequentially and explicitly (Amaziane, et al., 2008). These authors apply the scheme to flow and transport of radionuclides in a strongly heterogeneous porous medium as well as for a fractured 2D case. A comprehensive radionuclide transport study is also provided by (Bianchi, et al., 2015), who evaluate the effects of advective and diffusive processes in an excavated damage zone of a geological nuclear waste repository.

An important aspect of radionuclide transport is related to colloids. Review articles on colloid transport are given, for example, by (McCarthy, et al., 1989) or by (Malkovsky, et al., 2009). Essentially, mobile colloids in the subsurface environment may alter the transport of contaminants or, specifically, radionuclides. While the processes of colloid transport are enormously complex, the effective modelling approaches are relatively simple and linked often to sorption models, like Langmuir sorption. More advanced colloid transport models consider a particle's nonuniformity, which is introducing more and more model parameters that need to be represented and supported by specific data. Besides shape parameters for particles, this concerns also the partitioning between particles and radionuclides, which implies charges, and more generally the hydro-geochemistry. An interesting effect, which may be of particular relevance for the clearance of radioactive deposits, is described (among others) by (Knapp, et al., 2000). These authors show experimentally that, due to the Magnus effect, colloids tend to move in

the centre of a fracture flow (thus, also of a macropore flow field), which is why they travel in such cases rather with the maximum water velocity than with an averaged one. This may lead to colloid transport rates that are faster than the averaged flow. On the other hand, as for example discussed by (Moridis, et al., 2001), colloid particles are subject to different retardation effects like filtering, which essentially slows down their transport. Thus, colloid-transport models for the clearance need to be set up colloid-specific, scenario-specific, and nuclide-specific, thus requiring detailed data to derive meaningful conclusions for the clearance; as an exemplary reference see in (Bedrikovetsky, et al., 2011), who developed an extensive model for colloid transport with available experimental data. From this data, they obtained, for example, a detachment coefficient and other empirically derived model parameters for the colloidal transport. Also, the book on colloidal transport in porous media by (Frimmel, et al., 2007) emphasizes the important link between models and experimental data.

For different reasons, lack of time and lack of experimental data, colloidal transport was not addressed in this project. Instead, we propose to study this prominently and necessarily together with site-specific experimental work and data in future research. The literature review suggests that only in cases of very dominant preferential flow paths as in macropores, colloids may lead to a faster breakthrough of contaminants at a given sample point, say in a drinking water well as in the landfill scenario, which is later on addressed in this report.

The numerical simulator DuMu^x All implementations of the models introduced in this project were done in the research code and open-source numerical simulation platform DuMu^x. The name DuMu^x is short for “DUNE for multi- {phase, component, scale, physics, domain ...} flow and transport in porous media”. The core development team is the working group at the Department of Hydromechanics and Modelling of Hydrosystems (LH2) at the University of Stuttgart (Flemisch, et al., 2011), (Koch, et al., 2021), see also the website at dumux.org.

The objectives of the research at the LH2 department and collaborating institutions and their fields of applications indicate the direction of the development in DuMu^x. A variety of different topics have been covered in recent years, among which are, for example, radioactive waste disposal (Ahusborde, et al., 2015), CO2 storage in deep geological formations (Ahusborde, et al., 2015), (Hagemann, et al., 2016), (Nordbotten, et al., 2012), (Walter, et al., 2012), environmental remediation problems (Weishaupt, et al., 2016), fractured porous media in different applications (Gläser, et al., 2017), (Schwenck, et al., 2015), (Stadler, et al., 2012), (Tecklenburg, et al., 2016), karst research (Class, et al., 2021), and many more. Publications involving simulation results achieved with the DuMu^x simulator are found on puma.ub.unistuttgart.de/group/dumux.

As indicated before, DuMu^x is based on DUNE, the “Distributed and Unified Numerics Environment” (Bastian, et al., 2008), (Bastian, et al., 2008), (Bastian, et al., 2021), which is a “modular toolbox for solving partial differential equations (PDEs) with grid-based methods,” (dune-project.org). DuMu^x and DUNE use the object-oriented programming language C++ to achieve an optimal trade-off between generality and efficiency. The DUNE framework consists of several core and extension modules, which technically DuMu^x also is one of them. DuMu^x depends on all DUNE core modules and can inherit functionality from several DUNE extension modules.

The specific implementations linked to this project report will be publicly accessible on the dumux-pub platform: git.iws.uni-stuttgart.de/dumux-pub/winter2023a.

Instructions on how to download and install it are found in a README file in this module.

2 Model comparison regarding hydrodynamics in partially saturated porous media

In this chapter, we investigate the hydrodynamics of partially saturated flow in a heterogeneous domain, potentially with additional macropores. The main focus is on the comparison between approaches of different complexity regarding their physical assumptions. The problem is formulated for building rubble and debris of a nuclear power plant on top of a landfill. For example, it is aimed at assessing whether the flow in such a porous-media domain can be modelled with the Richards equation in sufficient accuracy or whether it has to be described by full two-phase flow equations that consider explicitly the flow of both water and gas phase. Furthermore, we investigate to which extent possibly occurring inertial effects should be added in the model in situations where higher Reynolds numbers play a role as, for example, in macropores. A big part of this work was also presented in (Winter, et al., 2022).

2.1 Governing equations

2.1.1 Mass balance

The flow of two immiscible fluid phases $\alpha \in \{w, n\}$ in a porous medium can be described on the Darcy scale by two mass balance equations

$$\frac{\partial(\phi \rho_\alpha S_\alpha)}{\partial t} + \nabla \cdot (\rho_\alpha \mathbf{v}_\alpha) - \rho_\alpha q_\alpha = 0; \ \alpha \in \{w, n\}, \tag{1}$$

with φ denoting the porosity, ρ_α the density of phase α, S_α the phase saturation, $\mathbf{v}_\alpha$ the Darcy velocity of phase α and q_α the phase source term (Bear, 1972), (Helmig, 1997). Equations (1) are usually complemented by a relationship for determining the capillary pressure $p_c = p_n - p_w$ as a function of saturation and the closure condition $S_w + S_n = 1$. This yields effectively two primary variables, where typically the pressure of one phase and the saturation of the respective other phase is selected.

Especially for water flow in an unsaturated porous medium such as the shallow subsurface, the full two-phase equations above can be simplified under the assumption of an infinitely mobile gas phase n. This assumption implies that the pressure of the gas phase is a static constant value over the whole domain of interest and that therefore, mass conservation only needs to be considered for the wetting phase w, namely,

$$\frac{\partial(\phi \rho_w S_w)}{\partial t} + \nabla \cdot (\rho_w \mathbf{v}_w) - \rho_w q_w = 0. \tag{2}$$

In this case, one can choose the water pressure pw as only primary variable and calculate the saturation using the inverse of the capillary pressure-saturation relationship. By converting pressure and saturation to hydraulic head and water content as well as inserting Darcy's law (3), the balance Eq. (2) can be cast into the typical form of Richards equation (Chen, et al., 1992), (Gerke, et al., 1993), (Nayagum, et al., 2004), (Rybak, 2016), (Šimůnek, et al., 2003). While Eq. (2) is actually implemented for the simulations performed in the course of the reported project, both forms are equivalent and we refer to Eq. (2) also as Richards equation.

2.1.2 Darcy's Law and Forchheimer's Law

The phase velocities v_α can be calculated using the multiphase extension of Darcy's law as follows:

$$v_\alpha = -\frac{k_{r\alpha}}{\mu_\alpha} \mathbf{K}(\nabla p_\alpha - \rho_\alpha g) \qquad [\mathrm{m\ s^{-1}}]; \ \alpha \in \{w, n\}, \tag{3}$$

with $k_{r\alpha}$ indicating the phase relative permeability, μ_α the phase mobility, **K** the intrinsic permeability, p_α the phase pressure and g the gravity vector. We note that we assume a rigid porous medium, namely, that the porosity and permeability distribution is fixed over time.

In cases where macropores are introduced in the domain, preferential flow may occur at significantly higher Reynolds numbers than allowed in typical Darcy regimes. Thus, such preferential flow might also include inertial effects (acceleration and deceleration in the pore throats). For such cases, the multiphase extension for Forchheimer's law

$$-(\nabla p_\alpha - \rho_\alpha g) = \frac{\mu_\alpha}{\mathbf{K} k_{r\alpha}} v_\alpha + \beta_\alpha \rho_\alpha \mathbf{v_\alpha} |\mathbf{v}_\alpha| \tag{4}$$

is an approach that has been used in literature (Fourar, et al., 2000), (Stadler, et al., 2012), (Sukop, et al., 2013), (Takhanov, 2011), (Wu, 2002), (Wu, et al., 2011) to describe higher Reynolds number flow regimes in porous media, fractured, or macroporous media and also for flow near well regions (Zhang, 2013), (Zhang, et al., 2012). It is a non-linear relation with second-order corrections and, thus, can be viewed as an extension of the linear Darcy law for higher velocity regimes (Sukop, et al., 2013). The non-linear term of the equation accounts for inertial effects and contains a coefficient β [m^{-1}], described as the effective non-Darcy-flow coefficient or Forchheimer coefficient. This coefficient is an empirical value, specific to the porous medium (Balhoff, et al., 2009), (Thauvin, et al., 1998), and has been a source of many controversies and ambiguities (Sobieski, et al., 2011).

The inertial coefficient varies with geometrical characteristics of the pore structure. Methods for computing β (see Eq. (5)) can be roughly split into two categories: (i) the first one is concerned with fitting measurement data directly to the assumed model, while (ii) another approach assumes a direct correlation of β to such fundamental properties of the porous medium as permeability (K), porosity (φ), and in some cases tortuosity (τ) (Sobieski, et al., 2011). The latter category can be further divided into theoretical and empirical correlations (Takhanov, 2011). The empirical correlations of the inertia coefficient were initially determined experimentally for single-phase flow (Wu, 2002). In order to account also for multiphase flow, they were extended in terms of saturation and effective permeability correction. This way, the corresponding change in the Forchheimer flow coefficient due to saturation difference can be described (Zhang, 2013). The β parameter values for typically studied porous media are reported to be greater than 5000 m^{-1} (Sukop, et al., 2013).

The flow velocities are calculated by the extended multiphase Darcy model, Eq. (3), or Forchheimer's model, Eq. (4), respectively. For Forchheimer's law, the Forchheimer coefficient is calculated with two approaches, thus, effectively, we consider two different Forchheimer models and evaluate their differences.

1. A generalized equation for all media (Nield, et al., 2008), which also is viable for multiphase flow, formulated here according to (Nuske, 2014):

$$\beta_\alpha = \frac{c_F}{\sqrt{K} k_{r\alpha}} \qquad [m^{-1}], \tag{5}$$

   where c_F is the so-called Forchheimer constant. A typical value of the constant for a range of investigated porous media can be 0.55 (Nield, et al., 2008). Other sources use much higher c_F values for their models. (Sobieski, et al., 2011) use values including other parameters and coefficients resulting in higher constants. They were able to perform measurements and gather data to fit these coefficients. In a recent student thesis (Keim, 2022), measured results of velocities at Reynolds numbers slightly above the Darcy range. He then tried to reproduce these with Navier-Stokes simulations, which obviously can model inertial effects, and then compared with a Darcy-Forchheimer approach. A reasonable agreement with the Navier-Stokes simulations could only be achieved with values of around c_F = 1000. Because of this wide range of values and without the help of measurements we decided to choose the widely accepted c_F = 0.55 for the macropore

comparison and test higher c_F values for the model area without macropores. The results are shown in Sec. 2.4.3.

If we insert Eq. (5) into the general form of the Forchheimer equation (4), we obtain the following equation for the first case:

$$\mathbf{v}_\alpha + c_F\sqrt{\mathbf{K}}\frac{\rho_\alpha}{\mu_\alpha}\mathbf{v}_\alpha|\mathbf{v}_\alpha| + \frac{\mathbf{K}k_{r\alpha}}{\mu_\alpha}(\nabla p_\alpha - \rho_\alpha \mathbf{g}) = 0. \quad (6)$$

2. An equation that accounts for multiphase flow more explicitly (Zhang, 2013):

$$\beta_\alpha = \frac{c_\beta \tau}{(\mathbf{K}k_{r\alpha})(\phi S_\alpha)} \quad [m^{-1}], \quad (7)$$

where c_β is a numerical constant which is found to be approximately equal to 1.5e-4 m for a specific range of investigated porous media (Zhang, 2013).

Again, by inserting this coefficient of Eq. (7) in the Forchheimer Law, we can write the velocity of the fluid phase α for the second case:

$$\mathbf{v}_\alpha + \frac{c_\beta \tau}{(\phi S_\alpha)}\frac{\rho_\alpha}{\mu_\alpha}\mathbf{v}_\alpha\mathbf{v}_\alpha + \frac{\mathbf{K}k_{r\alpha}}{\mu_\alpha}(\nabla p_\alpha - \rho_\alpha \mathbf{g}) = 0. \quad (8)$$

For each of the different models (based on Eqs. (3), (6) and (8), respectively), different macropore scenarios were simulated and the results compared with respect to their accuracy and also the efficiency of the simulations. Further, we study the relationships between the parameters of each model, and the inertia-affected flow is identified using the dimensionless flow criteria, i.e., Reynolds (Re) and Forchheimer (Fo) numbers (see Sec. 2.4.1).

2.2 The Setting of a Heterogeneous Landfill

In the landfills that we have in mind for this study, macropores are features that might potentially be present in a part of the soil/porous-medium volume. Even if they occur only very locally, they might dominate the flow and transport of water and solutes (Chen, et al., 1992) due to their irregular geometry and characteristics. Their effects on flow and how they can be described in state-of-the-art models, have intrigued the interest of many researchers. According to (Kumar, et al., 2017), macropore flow can be categorised as a flow phenomenon that is initiated from the soil (porous matrix) surface and terminated at the deeper profile or groundwater, bypassing the intermediate soil profile. Macropore flow is also denoted in literature as non-equilibrium and preferential (Beven, et al., 1982), (Christiansen, et al., 2004), (Kumar, et al., 2017), (National Research Council, 2001), (Šimůnek, et al., 2003).

For the following study, we selected a two-dimensional model domain, since the statistical approach we describe and use performs better in 2D than in 3D. Furthermore, we expect that the effects which we are interested in already occur in 2D and do not require a 3D setting. The model domain resembles a cut-out part from the middle of a landfill with the dimensions 10 m x 10 m. A cell length of 0.2 m has been chosen for the spatial discretization.

A major challenge in modelling landfills and their different materials as described above is the variation in their properties. Since it is impossible to predict the exact spatial distribution of the materials, we choose to create a spatial distribution with the R-project package gstat (Pebesma, et al., 2020), (R Core-Team, 2018). It requires to specify a variogram model, wherefore we choose the Matern covariance function

$$F(h) = \frac{1}{2^{\nu-1}\Gamma(\nu)}\left(\frac{h}{r}\right)^{\nu} K_\nu\left(\frac{h}{r}\right) \quad (9)$$

as available in gstat. According to (Minasny, et al., 2005), it works well for soil variograms. Its smoothness parameter ν, appearing in Eq. (9), allows for creating areas with less variation, which we assume

to be the case in the landfill. For more information about the Matern covariance function we refer to (Haskard, 2007). The parameters used are shown in the Appendix in Tab. A.2.

The most relevant spatial parameters for us are the porosity and the permeability. Since we are interested in macropores, we decided to create a porosity distribution with gstat and then relate the permeability with the Kozeny-Carman-relationship (Hommel, et al., 2018):

$$\mathbf{K} = \mathbf{K_{ref}} \frac{\phi^3(1 - \phi_{ref})^2}{\phi_{ref}^3(1 - \phi)^2}. \tag{10}$$

Here, we use a reference porosity φ_{ref} and a reference permeability $\mathbf{K}_{ref}$, which are calculated based on the grain-size distribution WT1 from the nuclear power plant Würgassen, published in (Müller, et al., 2007) and shown in Table 2.1. There, we also show the result for the mean particle diameter (l), which will be used in Section 2.4.1. Since the grain- size distribution is known, we are calculating the average particle diameter l as the weighted average of the range of diameters, namely,

$$l = \sum_{i=1}^{6} p_i d_i, \tag{11}$$

where d_i denotes an average fraction and the percentages p_i of the fractions are used as the weights of the average.

	fraction [mm]	average fraction d_i [mm]	percentage p_i [%]	weighted average $p_i d_i$ [mm]
1	< 2	1	3.8	0.038
2	2 - 4	3	3.7	0.111
3	4 - 8	6	9.6	0.576
4	8 - 16	12	15.8	1.896
5	16 - 32	24	41.3	9.912
6	32 - 64	48	25.8	12.384
l				≈ 25 mm

Table 2.1.: Calculation of weighted average (average particle diameter) based on the grain-size distribution.

The reference porosity is calculated as in (Cheng, et al., 2007), (Ishaku, et al., 2011), (Odong, 2007), (Sezer, et al., 2009), (Zhang, 2015) with the coefficient of grain uniformity

$$\eta = \frac{d_{60}}{d_{10}} \tag{12}$$

and the empirical relationship between φ and η, namely,

$$\phi = 0.255(1 + 0.83^{\eta}). \tag{13}$$

For this grain-size distribution it results in the reference porosity φ_{ref} = 0.35. The reference hydraulic conductivity is calculated after the Terzaghi equation (Cheng, et al., 2007)

$$k_f = C_t \left(\frac{\phi - 0.13}{\sqrt[3]{1-\phi}} \right)^2 d_{10}^2, \tag{14}$$

with C_t as the sorting coefficient, ranging between 6.1e-3 and 10.7e-3. Here, we choose the average value of 8.4e-3. Based on the grain-size distribution from Table 2.1 and the porosity calculated with Eq. (13), the resulting reference permeability is $\mathbf{K}_{ref}$ = 1.01e−9 m^2.

The entry pressure p_d [Pa] of the Brooks-Corey capillary pressure-saturation relationship,

$$p_c(S_e) = p_d S_e^{1/\lambda}, \tag{15}$$

is adjusted with the reference entry pressure $p_{d,ref}$ = 1000 Pa plus the spatially varying porosity and permeability using the Leverett J-function (Saadatpoor, et al., 2009) as

$$p_d = p_{d,ref} \sqrt{\frac{\phi \, K_{ref}}{\phi_{ref} \, K}}. \tag{16}$$

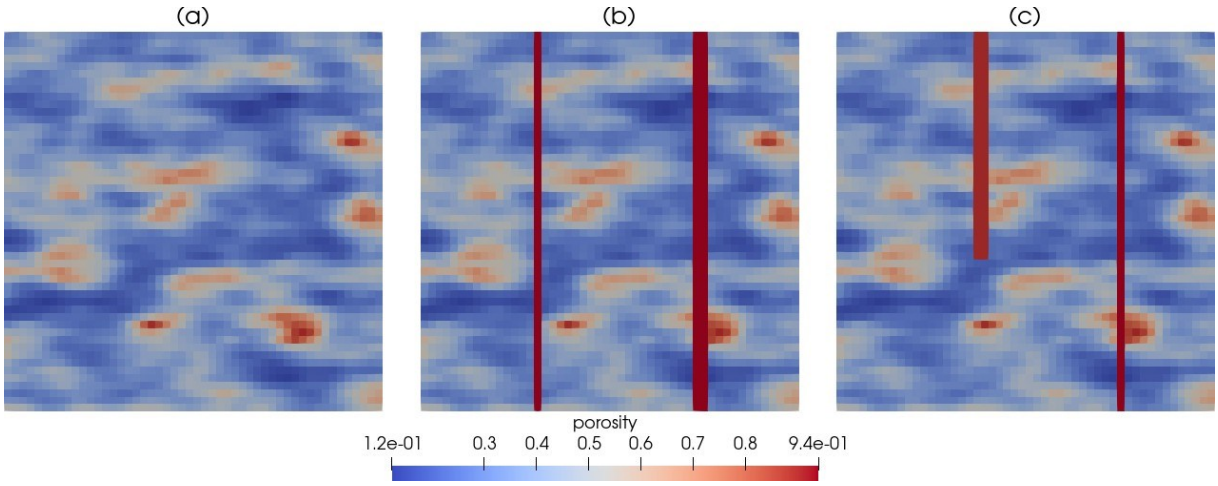

Figure 2.1.: The porosity fields for the three investigated cases: (a) no macropores (b) two macropores from top to bottom with different width (c) two macro- pores with different porosity and different width, only one from top to bottom.

From Eqs. (9), (10) and (16), we have calculated spatial distributions for the porosity, permeability, and capillary entry pressure. As macropores, we insert additional areas with very high porosity values (dimensions shown in Tab. A.1), and finally we end up with the porosity fields as shown in Fig. 2.1.

We assign Neumann no-flow boundary conditions at the left and right of the domain. At the top boundary, a Neumann boundary condition represents the in-flowing rain. Its mass is calculated from the official threshold for heavy-rain events q = 25 l m^{-2} h^{-1} = 0.07 kg m^{-2} s^{-1} provided by the German Weather Service (Deutscher Wetter Dienst). At the lower boundary, we set Dirichlet conditions with a fixed pressure and saturation.

The residual water saturation for the domain is set to $S_{wr,d}$ = 0.1, except for the macropores. Several studies (Dalla Valle, et al., 2017), (Kodešova, et al., 2006), (Stadler, et al., 2012) assume the residual saturation in the macropores to zero, namely, $S_{wr,m}$ = 0.0.

In Fig. 2.2 we show the porosity distribution histograms for the respective Scenarios (a), (b), and (c). The spikes at the tails of the latter two represent the high porosities assigned to the macropores. Obviously, this confirms the bimodal porosity behaviour of macroporous domains.

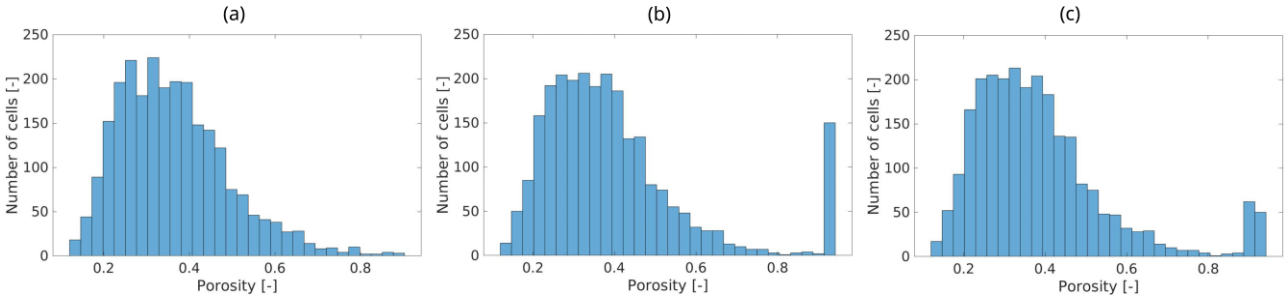

Figure 2.2.: Porosity histograms for Scenarios (a), (b) and (c). Every column depicts the number of cells for a porosity range $[\varphi_{min}, \varphi_{max})$ with $\Delta\varphi = 0.0275$. The total number of cells is 2500.

2.3 Richards versus Two-Phase equation - Results and Analysis

This section provides the comparison between the Richards equation, assuming an infinitely mobile gas phase, and the two-phase flow equations, considering viscous gas-phase flow, for the heterogeneous landfill setting as explained before. Scenario (a) without macropores is the basis for this comparison, see Fig. 2.1 (left).

2.3.1 Breakthrough curves

For the metrics to compare the two modelling approaches, we choose here the breakthrough profile curves. Note that this is not concentration over time, but rather the time of breakthrough over the bottom cross section. Breakthrough corresponds with the time at which the water saturation in the lowest domain cell reaches a threshold of ϵ = 1e-5 above the residual saturation.
The differences as seen in Fig. 2.3 are negligible between these two models. The earlier breakthrough in the centre, represented by the peak at around 5 m, can be explained by the regions of higher permeability along the vertical. Local trapping effects of the gas phase or any regions where viscous gas flow may slow down flow processes can- not be recognized from these results. This means, that for this particular setup, the simplification of the Richards equation can be justified.

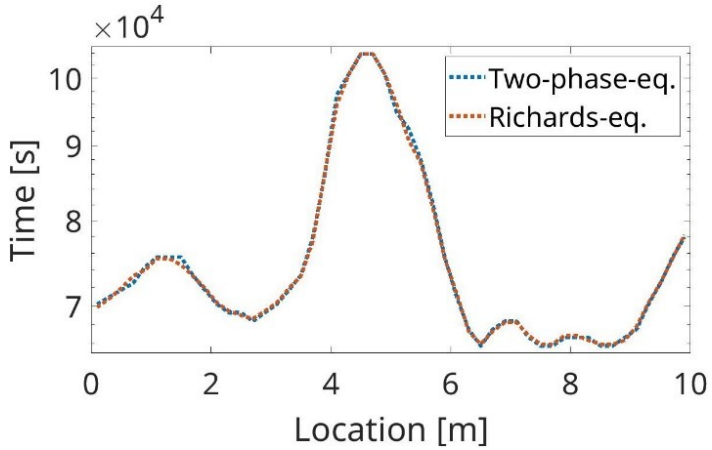

Figure 2.3.: Breakthrough comparison Richards and two-phase model

It might be different in cases where gas-saturations are locally trapped, for example, underneath a larger impermeable structure. Since this is completely speculative with respect to a variation of the settings in Fig. 2.1, we did not pursue this issue further given the time constraints in the project.

2.3.2 Numerical behaviour

	Total Time [s]	No. Global Timesteps	No. Newton Iterations	No. failed timestes
Richards	37.43	246	2034	0
Two-Phase	74.47	157	1267	4

Table 2.2.: Comparison of computational efforts and numerical behaviour for the Richards and two-phase-model.

The numerical behaviour of both models is shown in Tab. 2.2. The Richards model behaves not as good as the two-phase flow model in terms of numerical convergence,since it requires more time steps and Newton iterations. This is the case, because the inverse of the capillary pressure saturation relationship is used to calculate the existing saturation. For saturations close to 1, the gradient of the inverse is very steep, resulting in high saturation changes for small differences in capillary pressure, which effectively is less robust. However, since the Richards approach solves for one equation less, the total run time is still around only half of the time which the two-phase model requires.

2.4 Forchheimer vs Darcy - Results and Analysis

2.4.1 Flow-regime characterization

The Forchheimer number (see Eq. (18) below) represents the ratio of pressure drop caused by liquid-solid interactions to the pressure drop due to viscous resistance (Zeng, et al., 2006) and indicates how pore-scale effects in the porous-media structure lead to significant macroscopic (REV-/Darcy-scale) non-linear effects (Macini, et al., 2011). In porous media, there is no clear threshold number that defines the transition between the linear (Darcy) and the non-linear (Darcy-Forchheimer) flow regimes, and the non-linearity in non-Darcy flow is introduced from inertia due to strong local flow-path tortuosity rather than from turbulent effects. Therefore, in porous media, non-Darcy flow can occur for small Reynolds numbers (Zhang, 2013), i.e., below the occurrence of turbulence. Roughly speaking, creeping Darcy flow is observed for Re < 1 (Wang, et al., 2019). Non-Darcy inertial flow (or Forchheimer flow) occurs for a range of 1 < Re < 10 (Wang, et al., 2019). Furthermore, the critical Forchheimer number is between 0.005 and 0.2, as stated in (Zhang, 2013). Therefore, in this study we use the dimensionless Re and Fo-numbers as indicators for the prevailing flow regimes. Given their values, the required flow model can be chosen accordingly. This is why for the phase-velocity value we use the cell-data results from the Darcy models.

The Reynolds number Re is based on the average grain diameter (l) of Table 2.1 and the phase velocity,

$$\mathrm{Re} = \frac{|\mathbf{v}_\alpha|\rho_\alpha \mathrm{l}}{\mu_\alpha} \; [-], \tag{17}$$

which represents the ratio of inertial force to viscosity force. The Forchheimer number Fo has an expression that includes multiphase and inertia effects (Zhang, 2013),

$$\mathrm{Fo} = \frac{\rho_\alpha \mathrm{k} \mathrm{k}_{\mathrm{r}\alpha} \beta_\alpha \mathbf{v}_\alpha}{\mu_\alpha} \quad [-]; \; \alpha \in \{\mathrm{w}, \mathrm{n}\}, \tag{18}$$

where β_α is calculated from Eq. (7).

The non-Darcy effect (E) is the error caused by ignoring the non-Darcy behaviour. According to (Macini, et al., 2011), (Zeng, et al., 2006) is is defined as “the ratio of the pressure gradient consumed in overcoming the liquid-to-solid interactions to the total pressure gradient” and can be calculated as (Zeng, et al., 2006)

$$E = \frac{Fo}{1 + Fo}. \tag{19}$$

From this equation, we understand that the Forchheimer number is directly dependent on E. If we denote E_c as the critical value for the non-Darcy effect, then the critical Forchheimer number would be

$$Fo_c = \frac{E_c}{1 - E_c}. \tag{20}$$

For E_c = 10% (Shi, et al., 2018), (Zeng, et al., 2006) the critical Forchheimer number, or the lower limit for inertial flow to be considered, is equal to Fo_c = 0.11. This value is larger than the one given from literature and will be used as our critical Fo.

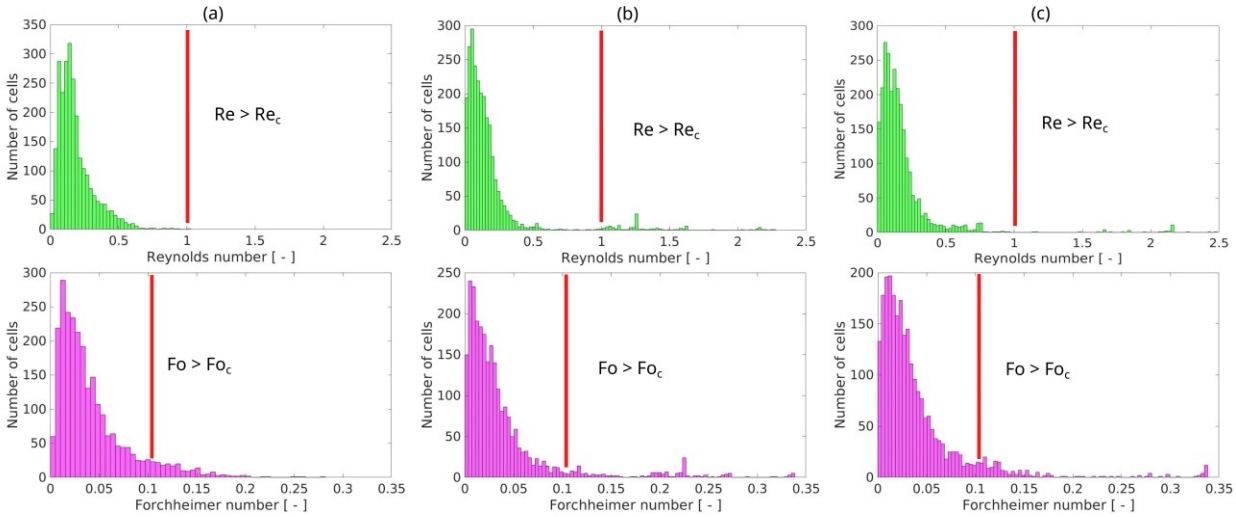

Figure 2.4.: Reynolds (Re, top) and Forchheimer (Fo, bottom) numbers histograms, calculated with the Darcy velocity values for the three scenarios (left to right). Every column depicts the number of cells for a range [Re/Fo_{min}, Re/Fo_{max}) with $\Delta Re/Fo$ = 0.009/0.003. The total number of cells is 2500. The critical Reynolds and Forchheimer numbers are depicted as red vertical lines.

In Fig. 2.4, we show the Reynolds and Forchheimer numbers for the three scenarios at the end of the simulation time. In Scenario (a), the Reynolds numbers barely reach up to Re = 1, with the majority of the domain in a smaller range of values. In Scenarios (b) and (c), where macropores are added, it reaches up to Re = 2.5. Again, the majority of the domain behaves like in Scenario (a), but we know that this variation of values at the tails of the histograms is caused by the macropores.
According to the typical range of the Forchheimer number for transition to inertial flow from the literature, all scenarios depicted here belong in the inertial regime. Even if we consider the "stricter" Fo_c = 0.11, we reach this limit already in Scenario(a). In Scenarios (b) and (c), the Forchheimer number reaches up to Fo = 0.35. We can see that with both dimensionless criteria, we have a large spread of values on the right tail for the macropore scenarios, along with some small spikes. We assume that these belong to the macroporous regions of the domain.
The results for the Forchheimer number confirm that the inertial effects are strong enough and they cannot be ignored in all three scenarios. The Reynolds criterionRe < 1 is only valid for Scenarios (b) and (c) in regions where flow is not affected by the macropores.

2.4.2 Velocity streamlines

In Fig. 2.5, we show the streamlines representing the water-phase velocity over the porosity fields for the two macropore scenarios after the last timestep. We present only the results for the Forchheimer - Case

1 model, as no significant differences between the others are visible. The strongest contribution of the macropores to the flow pattern is the preferential flow path they obviously offer. In both scenarios, we notice that the velocity streamlines around the macropores lead into them. This is caused by

- the different geometrical characteristics - continuous length and large width,
- the larger porosity and permeability compared to the rest of the domain and
- the residual saturation which is $S_{wr,m} = 0$.

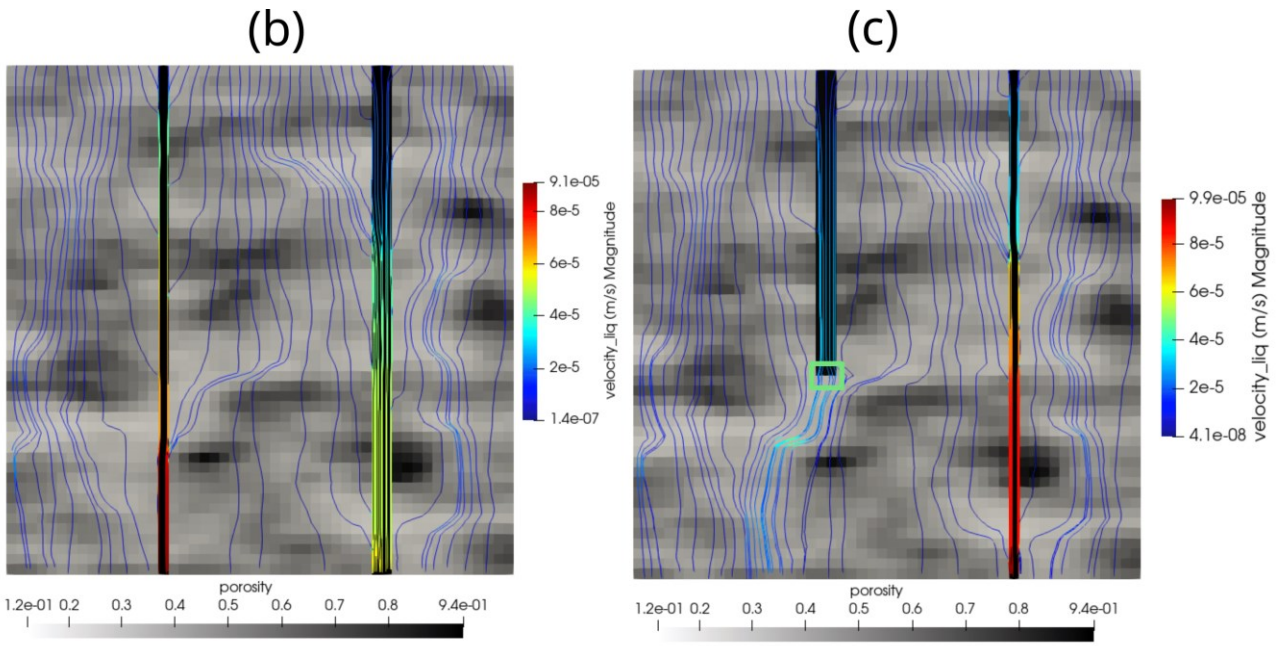

Figure 2.5.: Water phase velocity streamlines of Forchheimer - Case 1 model for Scenarios (b) and (c).

Moreover, the water-phase velocity in the macropores is considerably higher than in the rest of the domain. As we can see, in both scenarios the highest values occur in the thinner macropores, where we observe also a slightly higher pressure.
Between the three models used to simulate flow, the Forchheimer - Case 2 is the one that differs the most compared to the other two. We assume that the two cases differ the most in regards to the approach and consideration of the inertial effects. These should have the largest impact when the velocity is changing. To distinguish the two cases, we look into the green highlighted cells in Scenario (c), where the velocity isslowed down at the end of the left (wide) macropore.

	left cell	**right cell**
Macropore cells	2.47e-5	2.46e-5
Domain cells	1.87e-5	1.82e-5

Table 2.3.: Model liquid phase velocity results [m · s−1] for scenario (c) of Forchheimer- Case 1.

According to (Fourar, et al., 2005) and , (Ma, et al., 1993) the microscopic inertial effects at high velocities distort the flow lines and, therefore, increase the gradients of velocity and the pressure drop. Additionally, (Macini, et al., 2011) explains this with the dissipation of energy as fluid particles accelerate in smaller pores and decelerate while entering large pore spaces. As we study our cases, there should be a visible

faster acceleration or deceleration of water flow for the case with the higher inertial effect.

	left cell	right cell
Macropore cells	2.75e-5	2.75e-5
Domain cells	1.85e-5	1.80e-5

Table 2.4.: Model liquid phase velocity results [m · s−1] for scenario (c) of Forchheimer- Case 2.

In Tables 2.3 and 2.4, the velocities of the green highlighted cells in Fig. 2.5 are shown. The cells are the last in the macropore and the first afterwards. Generally, we can say that Case 2 has higher velocities in the macropores. Additionally, we can see that the velocity in Case 2 drops lower in the domain cells. If we follow the previously referenced literature, it would imply, that Case 2 accelerates and decelerates more than Case 1 and therefore has more inertial effects.

2.4.3 Breakthrough curves

Figures 2.6 and 2.7 show the breakthrough curves for all three scenarios. For the Scenarios (b) and (c), the macropores are dominating, which is best displayed on a logarithmic timescale. In the macropores themselves, there are also no significant differences, especially because the arrival times are so small.

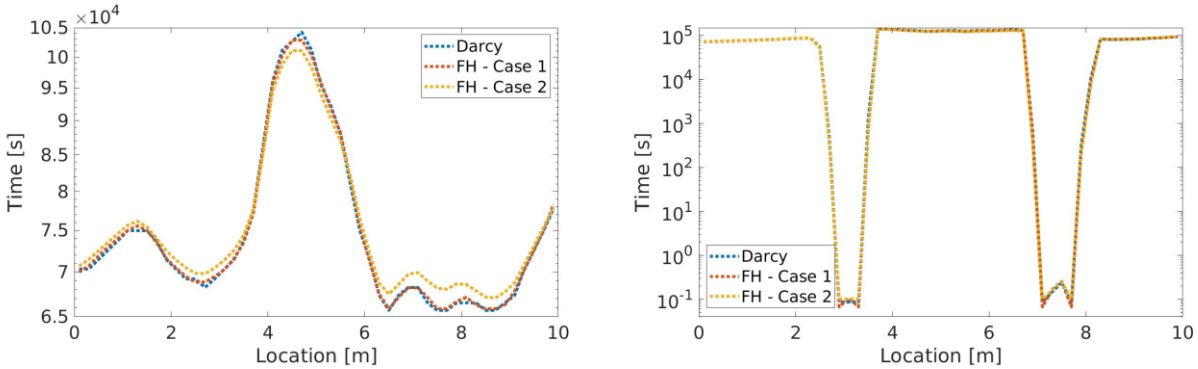

Figure 2.6.: Breakthrough curves for Scenario (a) and Scenario (b) and the three cases

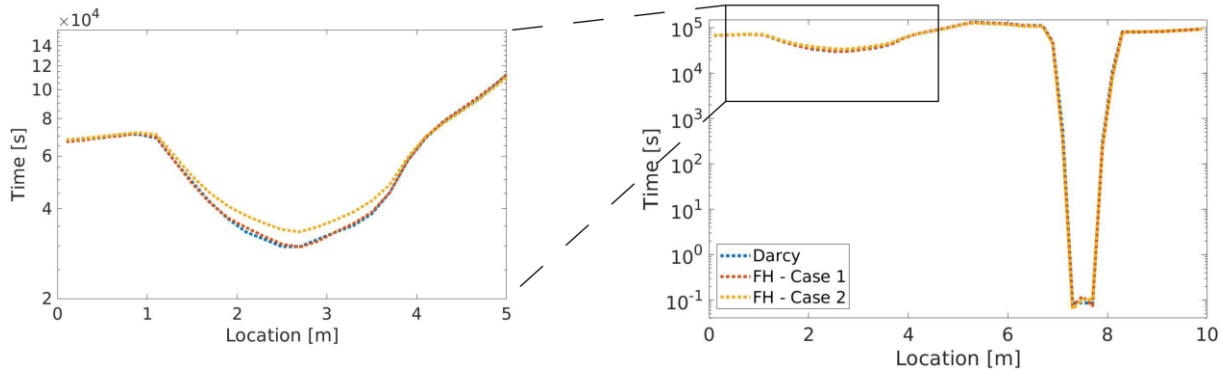

Figure 2.7.: Breakthrough curves for Scenario (c) and the three cases, with enlargement of the left macropore

The differences between the cases can be seen in Scenario (a) and the left macropore of Scenario (c), shown enlarged in Fig. 2.7. There, the Darcy model and the Forchheimer- Case 1 are very similar, while Case 2 clearly differs. In the areas where the water reaches the bottom faster, Case 2 is slower, while in the areas with a slower waterfront, Case 2 is faster. Since Case 1 is so similar to the Darcy model, this supports the approach of Case 2 having the Forchheimer coefficient with higher inertia effect. This was

also tested with higher influx boundary conditions, i.e. $q = 0.014$ kg m^{-2} s^{-1}. There, the differences between the models are more significant and the results are even more clear with regard to the acceleration and deceleration.

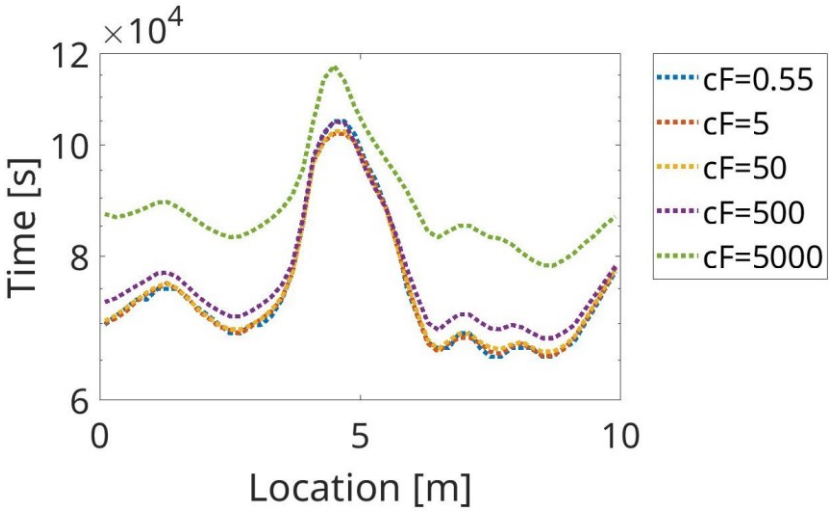

Figure 2.8.: Breakthrough curves for Scenario (a) and Case 1 and different c_F constants

As mentioned in Sec. 2.1.2, we additionally compared the differences between Darcy and Forchheimer approaches for $c_F > 0.55$. The results are shown in Fig. 2.8. As, of course, expected, the inertial effects increase for high c_F constants and can then become dominant. But without measurements or experiments to determine the coefficients like c_F or c_β needed in all the Forchheimer approaches it is difficult to justify deviating strongly from the literature and therefore impossible to make a definitive statement about the influence in a realistic setup without confirmation by data.

2.4.4 Numerical behaviour

In Tables 2.5, 2.6, and 2.7, the total runtime of the model simulations, the timesteps required for the solution, and the total of Newton iterations to solve the timesteps are listed for the implemented scenarios. A general observation for the Darcy and Forchheimer - Case 2 models is that the total runtime of the simulations decreases when the macropores, which induce faster flow, are added in the domain. More specifically, for both of them, the lowest total runtime occurs for Scenario (b) (Fig. 2.1). This may be explained by macropores being large areas in the domain where porosity, permeability, and entry pressure are constant.

	Total time [s]	**No. Global timesteps**	**No. Newton iterations**	**No. failed timesteps**
Darcy	57.08	121	1107	2
Forch. - Case 1	202.02	211	2009	1
Forch. - Case 2	1104.53	1274	12583	0

Table 2.5.: Computational effort and numerical behaviour for Scenario (a).

For the Forchheimer - Case 1 model, the total simulation runtime increases when the macropores are added (Tables 2.6 and 2.7). Interestingly, the longest simulation for this model is for Scenario (b), for which both the other models have their shortest runtime. This will be subject to further in-depth investigations beyond this report.

	Total time [s]	No. Global timesteps	No. Newton iterations	No. failed timesteps
Darcy	42.02	86	787	0
Forch. - Case 1	323.86	316	3019	9
Forch. - Case 2	905.74	1032	10159	6

Table 2.6.: Computational effort and numerical behaviour for Scenario (b).

	Total time [s]	No. Global timesteps	No. Newton iterations	No. failed timesteps
Darcy	48.30	98	907	0
Forch. - Case 1	290.04	316	2991	11
Forch. - Case 2	1003.27	1162	11442	7

Table 2.7.: Computational effort and numerical behaviour for Scenario (c).

2.4.5 Root-mean-square error(RMSE)

For our goal of comparing the two Forchheimer models and understanding their possible differences, we calculate the RMSE (root-mean-square error) for key parameters of the simulations (saturation [-], mobility [Pa^{-1} s^{-1}], and velocity [m s^{-1}]).
The RMSE is used to measure the error or the deviation of model-predicted results from observed values (Otto, S. A.). In our case, we want to measure the difference between the Forchheimer - Case 1 and Forchheimer - Case 2 results from the Darcy results. We use the Darcy results as our reference values and the results from the Forchheimer casesas the new values that need to be examined. We use the data of the final timestep.
The RMSE is calculated from the following equation (Otto, S. A.):

$$\mathrm{RMSE} = \sqrt{\sum_{i=1}^{n} \frac{(\hat{y}_i - y_i)^2}{n}}, \tag{21}$$

where $\hat{y}_i$ are the new values, y_i the reference values (Darcy model results) and n = 2500 the number of cell data pairs.

We compare the Darcy and Forchheimer models, using three different response parameters with different units or no units and different scales. That is why we calculate a normalized root-mean-square error (NRMSE), where we have a relative rather thanan absolute squared difference. We calculate our NRMSE by dividing the squared differences with the reference values (Otto, S. A.):

$$\mathrm{NRMSE} = \sqrt{\sum_{i=1}^{n} \frac{\left(\frac{\hat{y}_i - y_i}{y_i}\right)^2}{n}}. \tag{22}$$

From the results of the comparison between Darcy and the Forchheimer - Case 1 model (Tab. 2.8), we can see that the differences of Scenario (a) are a lot smaller compared to the rest and the respective differences of Darcy with the Forchheimer - Case 2. This would mean that the Darcy and Forchheimer Case 1 model are more in “agreement” for a heterogeneous domain when no macropores are added. For the rest of the scenarios, in both model differences we notice a similar tendency with the largest differences for the water-phase velocity and water-phase saturation parameters. The differences in saturation are a

result of the propagation of the flow field.

Case 1	Saturation [-]	Mobility [-]	Velocity [-]
Scenario (a)	2.61e-5	4.63e-4	9.50e-5
Scenario (b)	0.12e-2	1.90e-2	0.49e-2
Scenario (c)	0.16e-2	2.33e-2	1.28e-2

Table 2.8.: NRMSE values for the mobile (liquid) phase parameters between Darcy and Forchheimer - Case 1 models (t = TEnd).

Case 2	Saturation [-]	Mobility [-]	Velocity [-]
Scenario (a)	1.50e-2	2.27e-2	5.03e-2
Scenario (b)	1.18e-2	2.10e-1	6.07e-2
Scenario (c)	1.53e-2	2.40e-1	5.52e-2

Table 2.9.: NRMSE values for the mobile (liquid) phase parameters between Darcy and Forchheimer - Case 2 models (t = TEnd).

2.5 Discussion

In this chapter, we investigated flow in an unsaturated heterogeneous domain with and without macropores. The first topic focused on the comparison of the Richards-equation with the two-phase equation. For this setting, we did not identify major differences between the two approaches (see Fig. 2.3), even though we tried to introduce parameter distributions, from which we would expect to see effects like trapping, which would tend to violate the assumptions of the Richards equation.

Additionally, we investigated the mechanisms that affect flow and implemented three different model approaches. An extended multiphase Darcy model that simulates creeping flow and two multiphase Forchheimer models that consider the possible inertia effects. The Forchheimer models include a Forchheimer (inertia) coefficient which is subject of our investigation. Its calculation is mainly empirical, and the theoretic equations that exist vary depending on which parameters of the domain and the phases are included. Here, we use two equations to calculate it according to (Nuske, 2014), (Zhang, 2013). Regarding the final steady-state flow field, we can see from the breakthrough curves (Sec. 2.4.3), as well as from the velocity streamlines (Sec. 2.4.2), that the three models do not differ substantially. This shows that the two-phase flow problem is affected by the domain's characteristics (porosity, permeability), the traversing fluid's characteristics (saturation, relative permeability, mobility), and their interaction (capillary pressure).

The differences in the final velocity values are a result of the different approaches to the solution of velocity. The Forchheimer coefficient based on Eq. (5) depends on permeability and phase saturation via the relative permeability. On the other hand, in Eq. (7), the coefficient is directly proportional to tortuosity and inversely proportionalto permeability, relative permeability, porosity, and saturation. This is reflected in Fig. 2.9, where the beta-coefficient maps of both Forchheimer cases for Scenario (a) are shown. The distribution of the beta coefficient for Case 1 resembles the distribution of porosity and permeability and shows the same spatially smooth behaviour. Case 2 on the other hand is spatially more disrupted, even though also the areas with very high and very low porosity are visible.

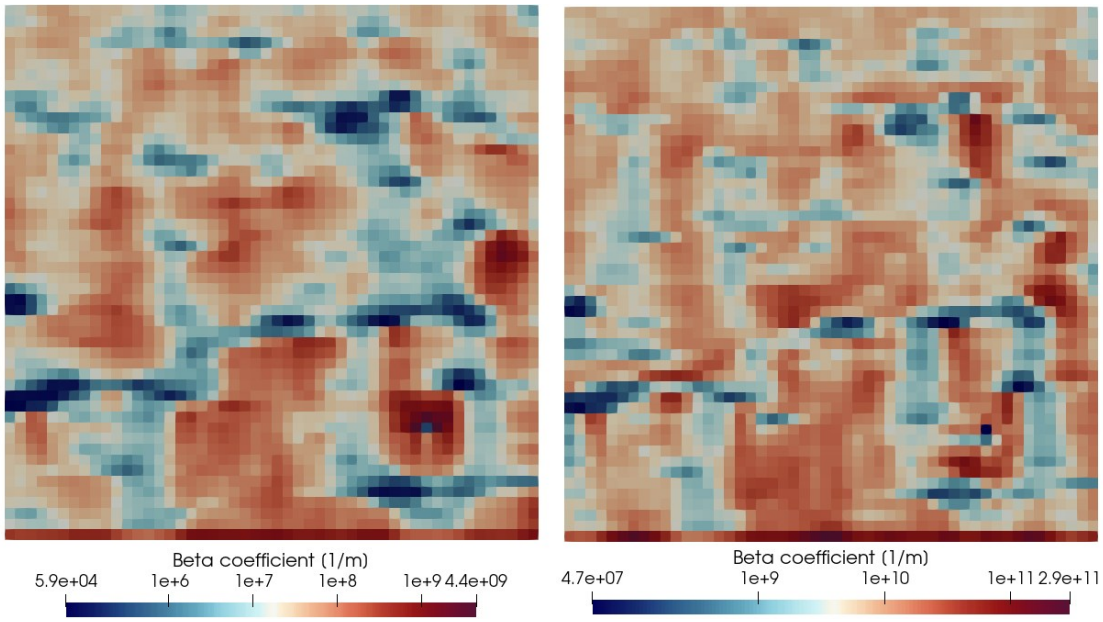

Figure 2.9.: Spatial Forchheimer coefficients for Scenario (a)

In Sections 2.4.2 and 2.4.3, we supposed that the Forchheimer - Case 2 has the higher inertial effects. This is also visible in Fig. 2.9, where the coefficient can become several orders of magnitude larger. This is probably influenced the most by the difference in how the permeability is considered in the calculation of the coefficient. In Case 1, it is with a square root, while in Case 2 not.
Since the context of this study is related to water flow and transport of low-level radioactive substances in landfills (Merk, 2012), the transient flow field is of high importance. This holds in particular since the differences between the breakthrough curves increase with higher velocities. Additionally, we keep in mind that in reality, macropores reaching from top all the way through to the bottom as in Scenario (b) should be unlikely. This puts more emphasis on the behaviour of the coefficients in Scenarios (a) and (c).
Choosing the "correct" Forchheimer coefficient for our case is de-facto impossible, since there are so many different possibilities with different parameters (Takhanov, 2011), (Thauvin, et al., 1998), (Zhang, 2013), for which we have currently no experimental data available. But we can conclude, that the coefficient for Case 1 needs less computing time and represents less inertial effects. In particular the differences to the Darcy model for Scenario (a), shown in Table 2.9, are marginal. If we follow our thought from above that the most interesting scenario is probably Scenario (a), we may conclude that using the Forchheimer equation with this coefficient is not appropriate and justified. It results in more computing time while providing no significant difference, even though we are above the critical Forchheimer number.

It is clear that the value of the Forchheimer coefficient depends critically on soil properties and hydrodynamic conditions, and it has to be determined for each individual case by comparison with experimental evidence. Thus, it is for now not possible to be conclusive in assessing the relevance of inertial effects, i.e., the necessity for the Forchheimer approach, in landfill settings as the ones we investigated here.
Motivated by flow events in heterogeneous landfills from debris of dismantled nuclear power plants, we investigated the differences between Darcy's law and the Forchheimer extension in the presence of macropores. Regarding the issue of Darcy vs Forchheimer approach, we reach the following conclusions:

- Based on numerical scenarios, which all featured Reynolds numbers beyond the validity of Darcy's law and, thus, an expected influence of inertia effects, we found that different approaches to calculating Forchheimer were showing different behaviour in representing inertia effects.

- At the same time the different investigated Forchheimer coefficients are associated with different

computational efforts.

— Dependent on the inflow boundary condition, the resulting velocities, and the size of the investigated domain, we could show that heterogeneous setups including macropores require the Forchheimer extension to account for inertial effects forthe transient transport solution.

— Macropores dominate the flow-field and the breakthrough times, in particular when they reach over large vertical distances, in this study from top to bottom.

3 Coupling hydrodynamics and mass transport

While the previous chapter dealt with different approaches to modelling the flow field in a landfill or in an aquifer, this chapter is concerned with the modelling of transport, i.e., with a radionuclide contamination that is transported with the flowing water phase or are subject to diffusion, adsorption, reactions, or decay. In Sec. 3.1, we present an implementation of a so-called tracer model. The term 'tracer' is employed in groundwater literature and commonly refers to substances that are in themselves rather foreign substances in the groundwater (de Vries, et al., 2002).

3.1 Tracer model

The tracer model in DuMu^x implements an approach which assumes that 'density and viscosity of the fluid phase in which the tracer gets transported are not affected bythe tracer', as described in the DuMu^x Documentation (Dumux Documentation). The concentrations of the radioactive contamination, which is considered in this study, are so small that the application of the tracer is justified. Thus, Eq. (23) describes tracer transport in the water phase:

$$\phi \frac{\partial \varrho X^\kappa}{\partial t} - \nabla \cdot \left(\varrho X^\kappa \mathbf{v}_f + \varrho D_{pm}^\kappa \nabla X^\kappa \right) = q, \tag{23}$$

with the dispersion coefficient for the porous medium D_{pm}

$$D_{pm}^\kappa = (\alpha_l - \alpha_t) \frac{\mathbf{v}_f \mathbf{v}_f^T}{|\mathbf{v}_f|} + \alpha_t |\mathbf{v}_f| \mathbf{I}, \tag{24}$$

after (Scheidegger, 1961).
The solution procedure requires that first the Richards equation or the two-phase flow equations are solved (see Ch. 2) to obtain velocities and saturations, upon which the transport of radioactive contamination is solved with the tracer model. In this strategy both the equations of the water flow and the tracer transport are solved implicitly each, while the coupling between them is sequential. Implicit means in this case, that the solution of the system of partial differential equations is solved implicitly in time, e.g. with a Newton scheme where the Jacobian matrix (stiffness matrix) is evaluated iteratively at the new time level. This leads to an unconditionally robust solution, while the computation is more expensive than an alternative explicit solution. The explicit scheme would use only the state of the system known from the former timestep, which means that the time step size must be limited by the Courant number, which is calculated from the cell length and the flow velocity. More explanations for the temporal discretization are presented in the DuMu^x handbook and documentation, which can be found here: https://dumux.org/docs/doxygen/master/.
This results in a computationally efficient, sequential and iterative solution strategy. The sequential use of the tracer model allows to compensate for a numerical challenge related to the extremely small values of realistic tracer concentrations, which are in the range of numerical truncation errors. The sequential tracer model allows for a scaling of the concentrations to higher numerical values without introducing undesired effects on the flow field.

3.2 Transport of radionuclides

3.2.1 Radioactive decay

A radioactive substance is unstable and decays with its half-life $t_{1/2}$ into a daughter with the same or a lower atomic mass number. The half-life indicates the time after which half of the currently present atoms are decayed. These generated daughter substances can also be radioactive, thus resulting to a so-called radioactive decay chain. All the members in the decay chain can have a half-life between less than a second and more than billions of years. Therefore, it is important to pay attention to the time scales of the simulations. Very rapid decay would require very small time-step sizes which is challenging for simulations that cover large time scales.

The radioactive decay is described by

$$\frac{dN}{dt} = -N\lambda, \tag{25}$$

with the decay rate $\lambda = \frac{\ln(2)}{t_{1/2}}$. This differential equation has the analytical solution

$$N(t) = N_0 e^{-\lambda t}. \tag{26}$$

This is included into Eq. 3.1 as source term:

$$\phi \frac{\partial \varrho X^\kappa}{\partial t} - \nabla \cdot \left(\varrho X^\kappa \mathbf{v}_f + \varrho D^\kappa_{pm} \nabla X^\kappa \right) = -\lambda X^\kappa. \tag{27}$$

In the DuMu^x code this source term is implemented as numerical solution by

$$\Delta N_{t_1} = - N_{t_0} \lambda \Delta t_{t_1 - t_0}. \tag{28}$$

The numerical implementation as in Eq. (28) has been compared with the analytic solution in Eq. (26). The results are given in Tab. 3.1 for ^{129}I, which has a stable daughter nuclide. The solutions are calculated zero-dimensional in a single cell without in- and outflow, and the end time TEnd was set to the half-life of the substance, thus facilitating the check of the result. The comparison between analytical and numerical solution was performed with different maximum timestep-sizes, Δt_{max}, in the numerical model. The initial concentration is large compared with values that could realistically be expected, which further tends to minimize possible numerical truncation effects on the results. The differences shown in the table are evaluated for the end time of the simulation.

Δt_{max}	**No. Timesteps**	**ΔAnalytic-Numeric**	**Δ Analytic-Numeric per current conc.**
1e10	50.000	9e4	1.8e-5
1e11	5.000	9.4e5	1.88e-4
1e12	500	4.4e7	8.8e-3
1e13	50	1.3e8	2.6e-2

Table 3.1.: Difference between analytic and numerical solution for different maximumtime step sizes for ^{129}I with half-life (and TEnd) = 4.95e14 s and initial concentration of 1e10

As Tab. 3.1 shows, the relative errors are small but they increase as the allowed time-step size increases relative to the half-life. This means that for each implemented radioactive decay model, one has to be aware of the errors inherent to numerically solving the decay.

Furthermore, the numerical solution was checked for a decay chain with two radioactive daughter elements: ^{90}Sr with its radioactive daughter ^{90}Y. Their half-lifes are 911390400 s and 230000 s, respectively. Therefore, the maximum time-step size was set to the half-life of ^{90}Y.

For the daughter species, the analytical solution of Eq. (26) is not valid. Instead, the analytical Bateman solution formula provided in (Harr, 2007) was employed:

$$N_2(t) = \lambda_1 N_1(0) \left(\frac{e^{-\lambda_1 t}}{\lambda_2 - \lambda_1} + \frac{e^{-\lambda_2 t}}{\lambda_1 - \lambda_2} \right). \tag{29}$$

Substance	Δ Analytic-Numeric	Δ Analytic-Numeric per current conc.
^{90}Sr	3.3e7	6.7e-3
^{90}Y	8.4e3	6.46e-3

Table 3.2.: Results of decay of ^{90}Sr and ^{90}Y with TEnd = 911390400 s and time-stepsize of 230000 s, resulting in around 4000 time steps

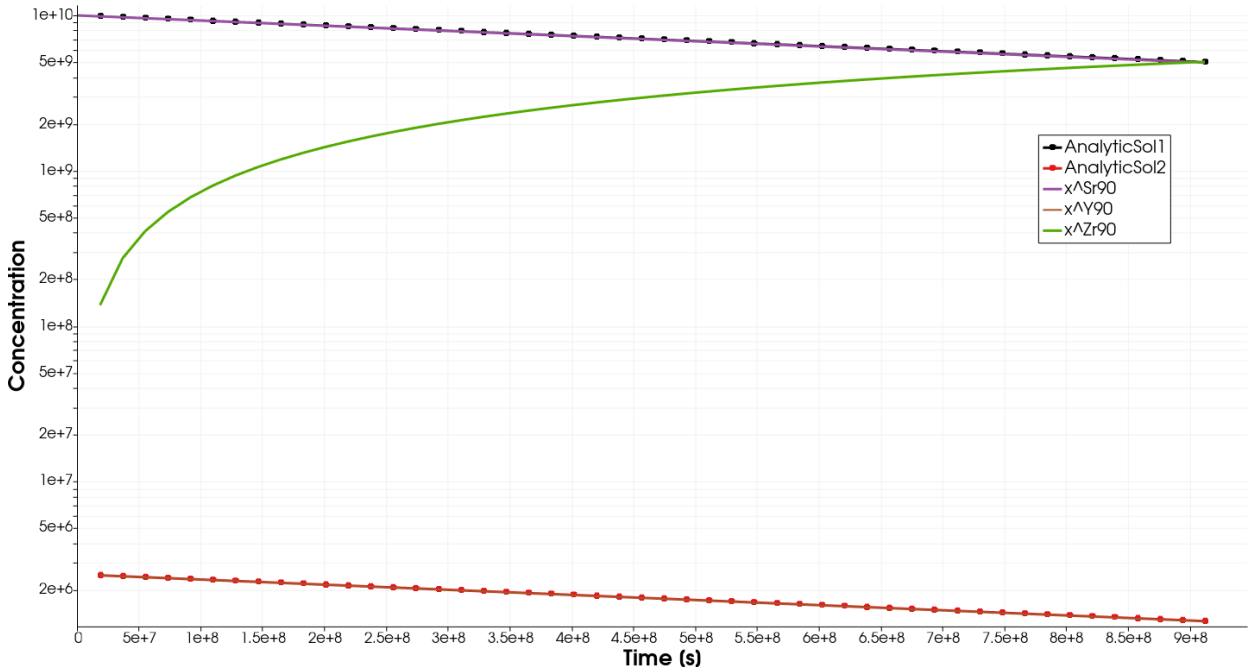

Figure 3.1.: Decay model (numerical) of ^{90}Sr and ^{90}Y compared with their analyticsolutions over time

3.2.2 Sorption

Sorption describes the process of a substance adsorbing to another, here: solid, substance, mainly the solid matrix. Dependent on the adsorbed amounts and the concentration in the aqueous phase, adsorbed substances can also desorb again back into the fluid. A very common approach to modelling sorption processes is the usage of the partition coefficient K_d. It is defined as the quotient of the mass of sorbed adsorbate A_i and the mass of the adsorbate in solution C_i (U.S. Environmental Protection Agency, 1999):

$$K_d = \frac{A_i}{C_i}. \tag{30}$$

There is a lot of literature dealing with the measurement or determination of these $K_d$values for adsorbates and sorbates; authors commonly agree that K_d values can vary over several orders of magnitudes (U.S. Environmental Protection Agency, 1999), (U.S. Environmental Protection Agency, 1999), (U.S. Environmental Protection Agency, 1999).
To include sorption, we add a solid phase to the storage term. Beforehand, the term could be shortened, but now we also have to include the density ϱ_w and the saturation S_w of water, since multiple phases are considered:

$$\frac{\partial(\varrho_w \phi S_w X_w^\kappa + \varrho_b X_s^\kappa)}{\partial t} - \nabla \cdot \left(\varrho_w X_w^\kappa \mathbf{v}_f + \varrho_w \phi S_w D_{pm}^\kappa \nabla X_w^\kappa\right) = -\lambda \varrho_w \phi S_w X_w^\kappa - \lambda \varrho_b X_s^\kappa. \tag{31}$$

Then, the solid concentration X^κ can be substituted with the K_d approach using $X_s^K = K_d X_w^K$. This

leads to:

$$\frac{\partial(\varrho_w \phi S_w X_w^\kappa + \varrho_b K_d X_w^\kappa)}{\partial t} - \nabla \cdot \left(\varrho_w X_w^\kappa \mathbf{v}_f + \varrho_w \phi S_w D_{pm}^\kappa \nabla X_w^\kappa\right) = -\lambda \varrho_w \phi S_w X_w^\kappa - \lambda \varrho_b K_d X_w^\kappa. \tag{32}$$

An extension of this concept is the 'smart-K_d' approach presented in (HZDR, et al., 2018), (Stockmann, et al., 2017). Before running the models, a matrix of K_d values for a range of properties like pH-value or temperature is created. Then, dependent on the conditions, the correct K_d value is chosen. For this work, the 'classical' K_d-approach is applied.

4 Modelling the Water Pathway of Radionuclide Transport in a Landfill/Groundwater Scenario

A major goal of this project is a comprehensive analysis of the water pathway as outlined in the IAEA Safety Report 44 for radionuclides. This involves transport with the water, induced by rain events on a landfill, through the unsaturated porous medium in the landfill and the saturated zone of an aquifer. The modelling approaches regarding the hydrodynamics and the transport of radionuclides, as explained in the previous chapters, can be flexibly applied with the DuMu^x simulator to study the effects of different scenario assumptions as well as of various parameters and processes. Doing so allows for outlining the band width of predictions with respect to concentrations in a hypothetical well at a given distance.
We note that this chapter does not provide a comprehensive and systematic uncertainty analysis. This could unfortunately not be achieved within the duration of the project, but is planned to be completed in ongoing work after the project.

4.1 The Scenario

From the schematic sketch as presented by (Merk, 2012), shown here in Fig. 4.1, a 1D setup can be derived, as it was done also by (Merk, 2012). It represents the landfill body and the vadose zone underneath in 1D with a homogeneous porosity and permeability. Below the landfill, the transport through the aquifer to a well (the protected good in this scenario) in 500 m downstream is also modelled by these authors in 1D. (Merk, 2012) in fact, employed two 1D models and exchanged the information between those with an external interface. Here, we have realized the implementation in a single model setup as quasi-1D. In fact, the model is 2D, but the respective area is only one discrete cell in width, such that, effectively, flow is calculated in only one dimension. As a result, the model domain looks like an 'L'-shape. The assignment of the boundary conditions follows Fig. 4.1. On the top of the landfill, a Neumann boundary condition with a sinusoidal rain profile over a year is assigned, with an incoming rain of 0.8 m/y. On the left side of the aquifer, there is a Neumann boundary condition for representing the inflowing groundwater, and on the right side of the aquifer, a Dirichlet condition is given (in terms of head) for the outflowing groundwater. The remaining boundary conditions are no-flow Neumann. As contamination we use from now on the iodine isotope ^{129}I, which is considered to be an important radionuclide (Merk, 2012).

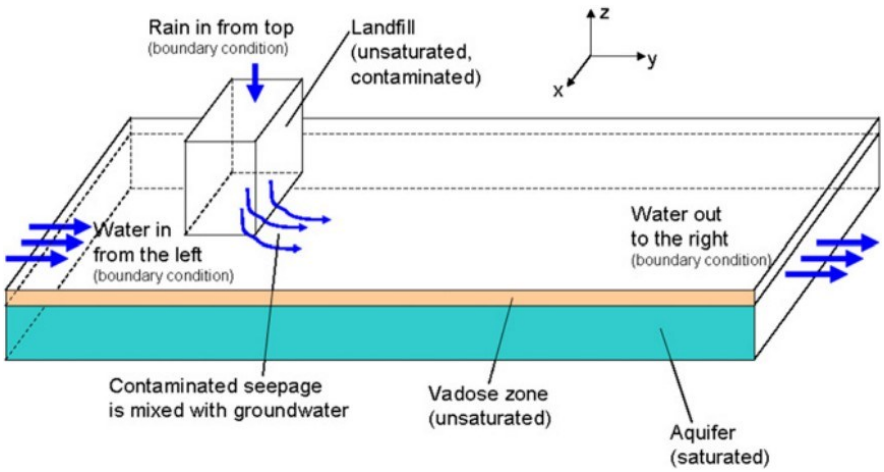

Figure 4.1.: Setup with two 1D-models from (Merk, 2012)

We expect that the 1D analysis of the transport scenario for radionuclides from the hypothesized landfill tends to overestimate the concentration of contaminants arriving at the well. A dilution into perpendicular directions is not possible. Thus, we expect that the 1D scenario is conservative in assessing the risk of contaminant concentrations in the drinking water well. In order to account for

the aspect of dimensionality and to get a better understanding of the amount of overestimation, it is useful to compare the 1D scenario with a 3D scenario.
Thus, the 1D domain is extended into a setup for a 3D case for the Sec. 4.3. Again,we choose the dimensions and soil parameters as presented in (Merk, 2012) for the 1D scenario. There, the surface of the landfill is 300 m x 300 m. The 500 m to the well are measured from the downstream edge of the landfill. Additionally, to create a more realistic profile for the landfill, we have chosen to let the length and the width increase. To the sides, an additional 100 m are added, which is intended to minimize effects from interactions with the boundary conditions. The boundary conditions are the same as before, except for the Neumann boundary condition on the top, which is not restricted to the landfill. The resulting domain, as shown in Fig. 4.2, is used in Sec. 4.3. Our well is now at x = 950 m, because the pyramid scheme adds another 50 m.

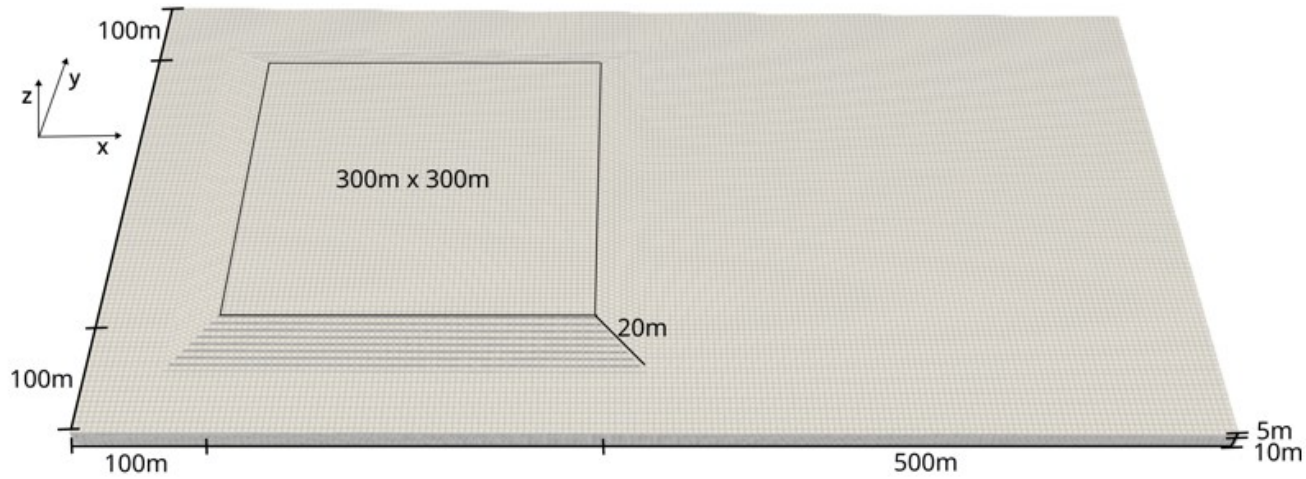

Figure 4.2.: 3D model domain

4.2 1D Results

As already mentioned, the study of (Merk, 2012) serves as the reference for the extended numerical simulations in this project on radionuclide transport along the water pathway. Thus, we compare the results of Merk with those obtained with the DuMu^x simulator and the equations as explained in the previous chapters. The modelling approaches differ in some details and assumptions, and for that reason an exact reproduction of the results is beyond the scope of this project.
Therefore, the setup of the landfill, the vadose zone, and the aquifer underneath as well as their physical parameters are copied from Merk. In Fig. 4.3, the results ofthe scenario with a contamination with ^{129}I are compared, where in this particular case different K_d values were used. The K_d values have the SI unit m^3/kg. The plot illustrates the concentration over time at the well 500 m in downstream flow direction of the aquifer. A front reaching the well after a certain time can be observed, with the arrival time and shape of the curve dependent on the K_d value. Generally speaking, the higher the K_d value the more influence the sorption has and the later the front reaches the well. The oscillatory ups and downs in the curves result from the sinusoidal rain profile applied in the form of a Neumann boundary condition for the water mass balance as mentioned in Sec. 4.1. It can be easily seen that the DuMu^x and Hydrus results differ quite significantly from each other. The arrival fronts are very close to each other in all instances, which confirms that the groundwater flow is represented consistently in both models. However, the concentration peaks modelled by the DuMu^x simulations are at lower values, and the concentration drops faster. Since this is consistently observed for all the simulated cases, we suggest that this has its origin in a systematic difference between the two approaches. One explanation for the deviations is the different setup of our monolithic quasi-1D DuMu^x model as compared to the sequential arrangement of two 1D models in (Merk, 2012). Also, we noticed differences in our results for varying refinements in the vertical landfill column, which is why an in-depth comparison study

would need to focus on grid-converged results besides the coupling scheme.

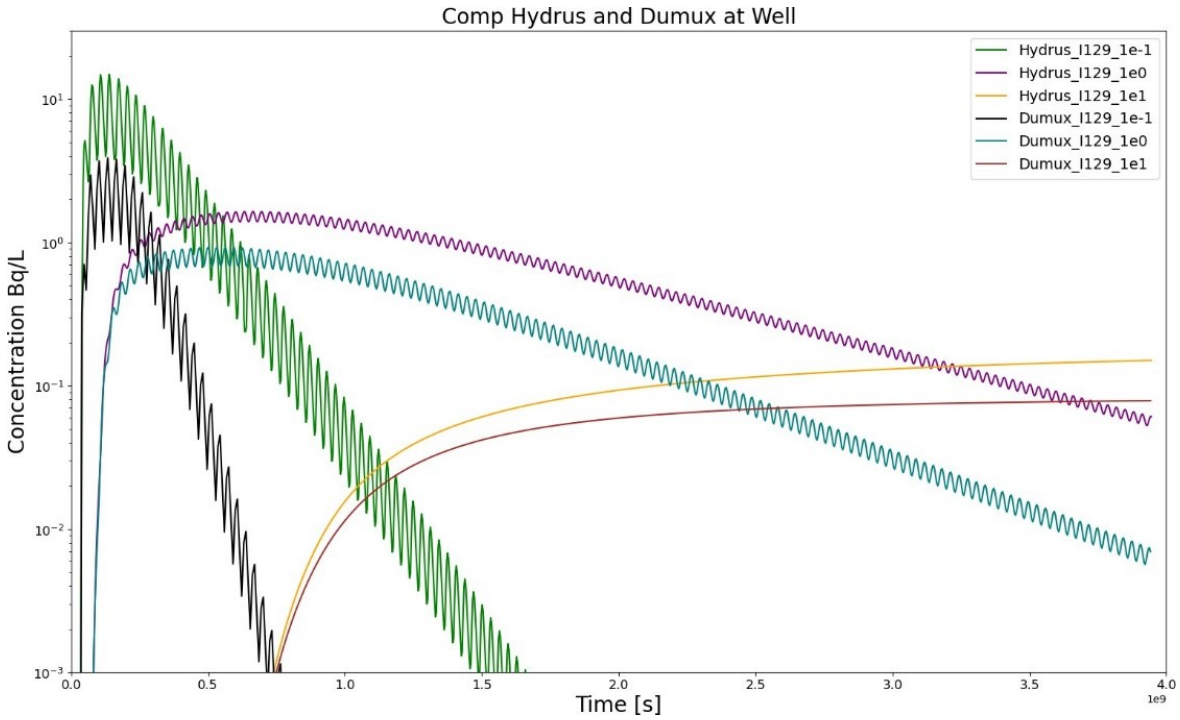

Figure 4.3.: Concentration of the ^{129}I over time at the outlet of the aquifer 500 m after the landfill in comparison to (Merk, 2012) (for the latter, these are the curves labelled with Hydrus... in the legend)

Fig. 4.5 shows that grid-convergence for the DuMu^x runs is obtained with decreasing cell-lengths, while the refinement results in a steeper gradient of the radionuclide concentration over the height of the landfill body. Thus, the concentration flowing into the aquifer is different dependent on mesh resolution. This leads to the differences inthe concentrations at a given downstream point over time as shown in Fig. 4.4. We did not investigate further the grid resolution used in (Merk, 2012) and cannot draw conclusive insights in this regard.

Further explanations for deviations between the DuMu^x 1D model and the Merk study might be found in specific differences between the two software packages (DuMu^x and Hydrus). Thus, we tested them in a comparison for a more simplified test. For that we used a 1D column as simple setup, similar to the one we described in Chapter 4, but here without the coupling to the aquifer. On the top of the domain, a Neumann(flux) boundary condition for the water is applied and a Dirichlet boundary condition for the tracer to fix the tracer's concentration at the top. This results in a water inflow transporting tracer into the domain. On the bottom of the domain, we have a Dirichlet boundary condition to allow for the outflow of both water and tracer.

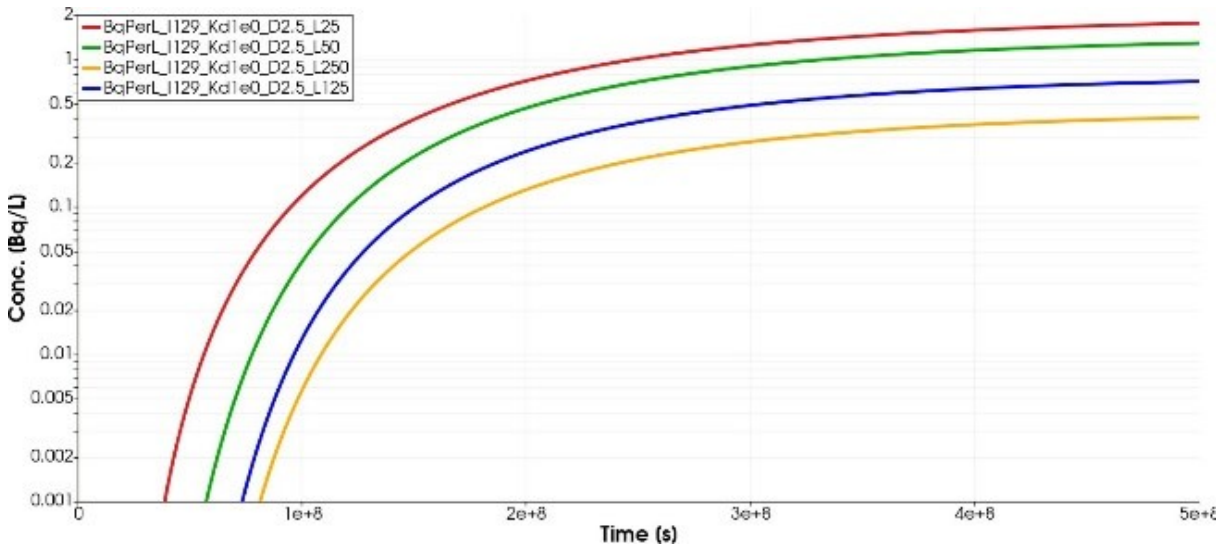

Figure 4.4.: Differences on the model output resulting from varying refinements in vertical direction over the time

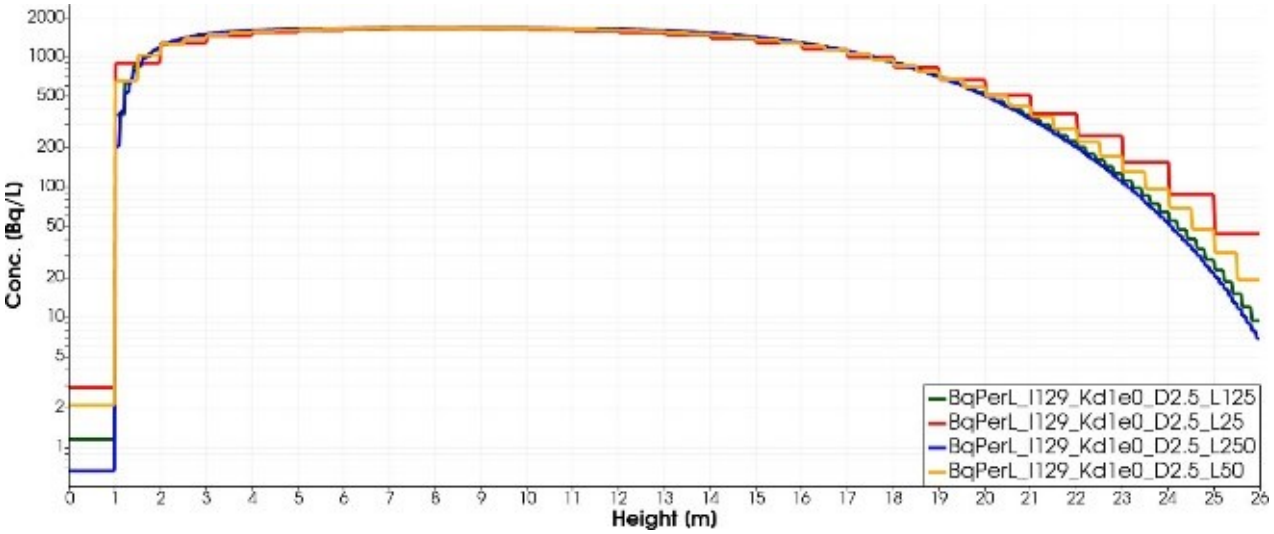

Figure 4.5.: Differences on the model output resulting from varying refinements in vertical direction over the height

For the DuMu^x versus HYDRUS comparison, we focus on the water flow calculated with the Richards equation as well as the tracer; while we do not include sorption or decay, only dispersion is considered. Fig. 4.6 shows the water content over the column height for different timesteps and for both simulators. The different maximum water content is a result from inaccuracies when converting the Van-Genuchten-Mualem parameters used in Hydrus to the Van-Genuchten parameters in DuMu^x. Besides that, there are small differences in the propagation of the water front, but we assume that this also could be due to the difference in the maximum water content.

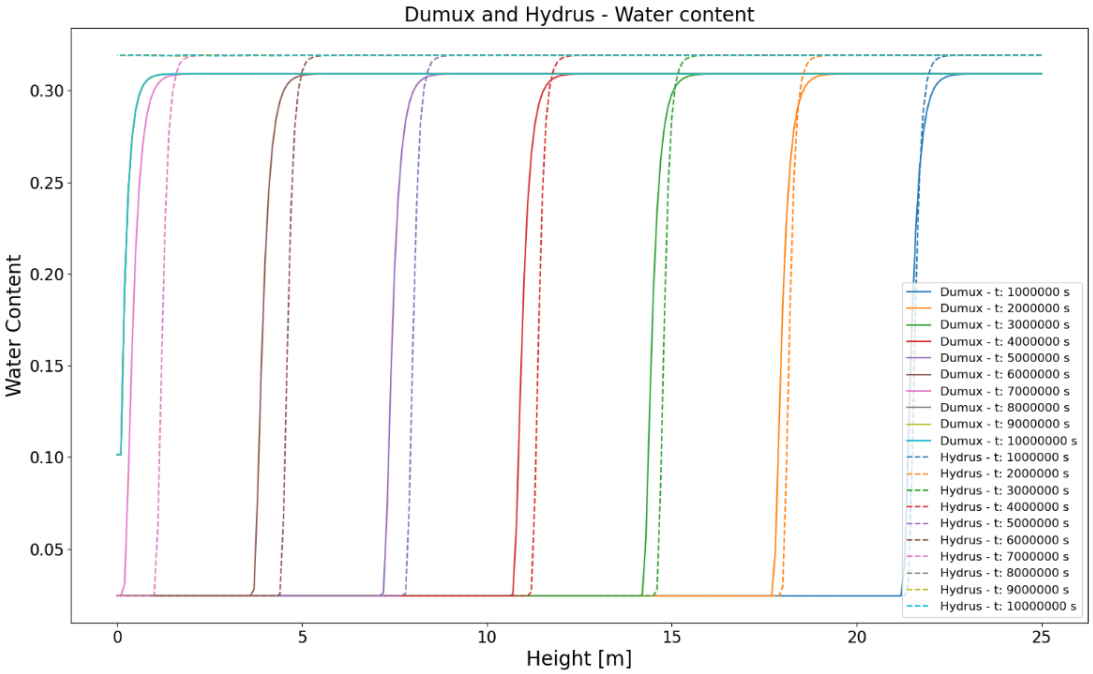

Figure 4.6.: Water content over the column height for DuMu^x and Hydrus

In Fig. 4.7, the tracer concentration at different points in time is shown. We can see the same differences in the tracer front as in Fig. 4.6 and additionally a characteristic difference in the kink which is seen in the tracer concentration profile. Overall, in spite of these obvious differences, the results are still very good in qualitative and with some restrictions also in quantitative agreement to each other. For that reason, we will use in the following sections the DuMu^x 1D model as the reference model in 1D to investigate further effects like number of spatial dimensions considered in the model approach or the effects to be expected due to changes in rain events that drive the transport of radionuclides through the landfill body, which may then be linked to predictions due to climate change.

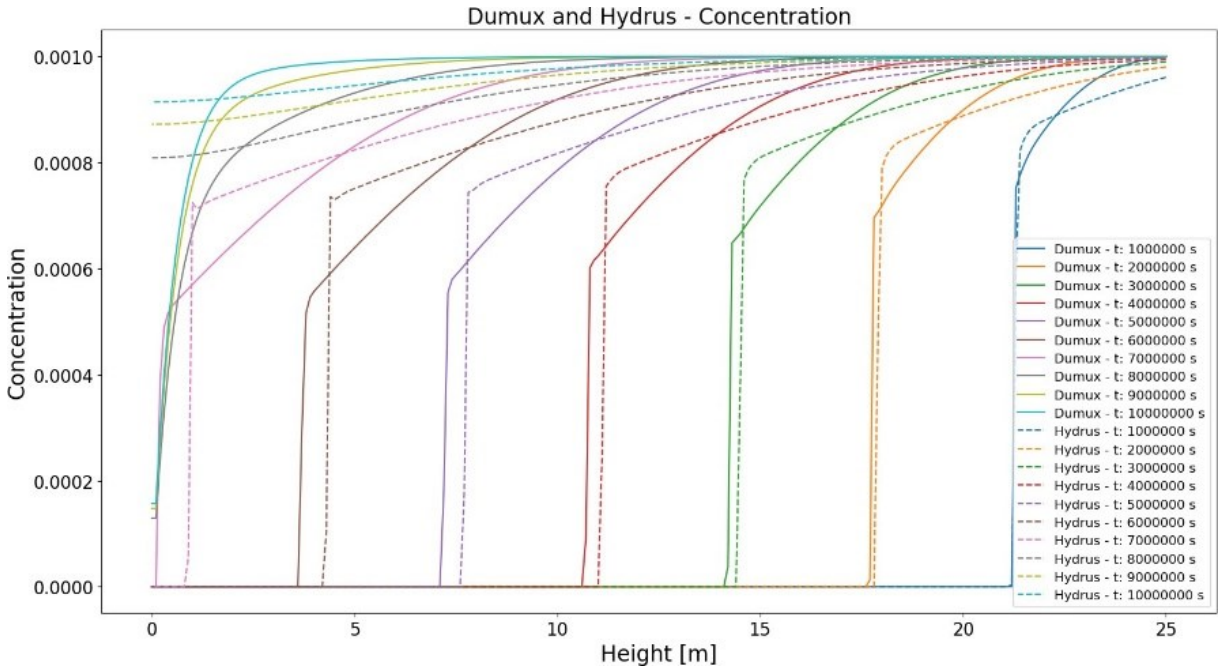

Figure 4.7.: Tracer concentration over the column height for DuMu^x and Hydrus

4.3 3D Results and Comparison to the 1D Simplification

In this section, we present a model scenario, as previously used for the 1D simulations, which is now extended to three dimension, see also in Sec. 4.1. The parameters characterizing the scenario remain the same as in the 1D case; thus, the differences between the models could be due to the different dimensions in the models, which is also linked to a description of the boundary conditions implying a significantly higher complexity in a 3D model. For example, the Neumann flux condition for rain on top of the landfill has to be applied now for the entire top boundary of the 3D model domain, or the flux in the groundwater aquifer cannot be simply described (as in 1D) by a fixed flow as in a Neumann flux condition; instead, it has to fit to the pressure profile in the modelled unsaturated zone, etc. For this comparison we chose a K_d-value of 1e-4 m^3/kg.
Due to the infiltration from the landfill body and the coupled aquifer flow, the lateral flow and contaminant transport takes mainly place at the top of the aquifer at z =10 m. A vertical spreading and distribution of the radionuclides across the thickness of the aquifer happens due to dispersion the further we go in downstream direction. However, at a distance of several hundreds of meters from the landfill, as shown in this landfill/aquifer water-pathway scenario, there is still a very dominant concentration peak in the uppermost cell of the aquifer.
In the early times of the simulation runs, we observe that radionuclides are washed out faster into the aquifer towards the outer sides of the step-shaped/pyramid-shaped land fill body than from its centre parts. This is important to note in order to comprehend and contextualize the results in the comparison with the 1D results. At these step- shaped pyramid slopes, the rain from the top needs less time to transport the tracer into the aquifer. Thus, the response to rain events, modelled as boundary conditions, is much quicker. Representative for this period we show the developing contamination plume as a contour plot in Fig. 4.8 and in line plots in the cross section of the aquifer in y-direction at z = 10 m and different times in Fig. 4.9.

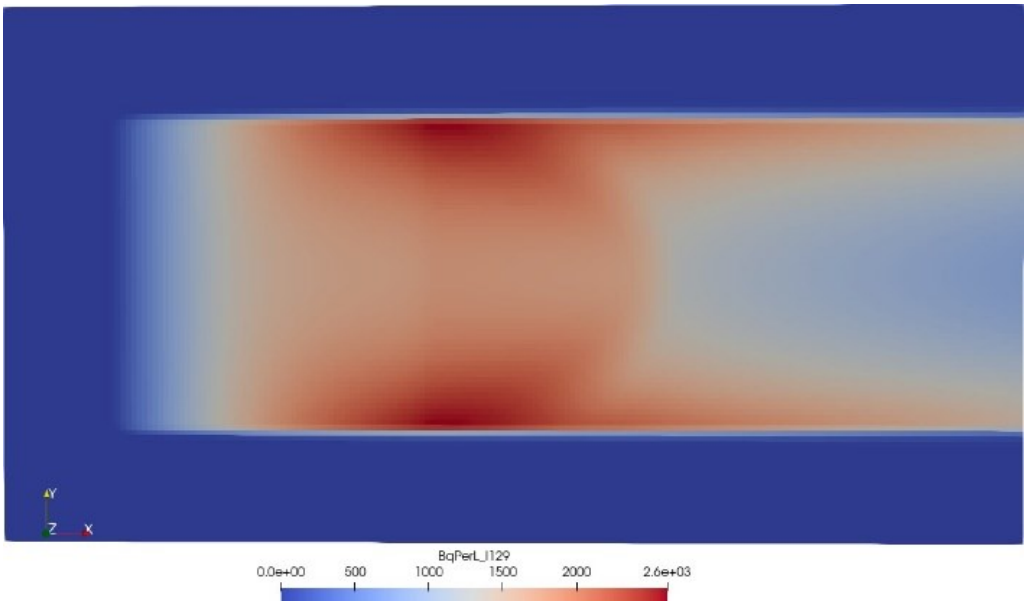

Figure 4.8.: Concentration plume at z = 10 m and t = 1.2e8 s

Upon this initial period featuring the radionuclide intrusion from the lateral sides of the landfill pyramid, the landfill is washed out continuously with a much less prominent concentration peak in the middle at later times, which is explained by the transversal dispersion transporting the contamination towards the centre and levelling out concentration gradients in the cross section. The plume and cross section are shown in Fig. 4.9 and Fig. 4.10.

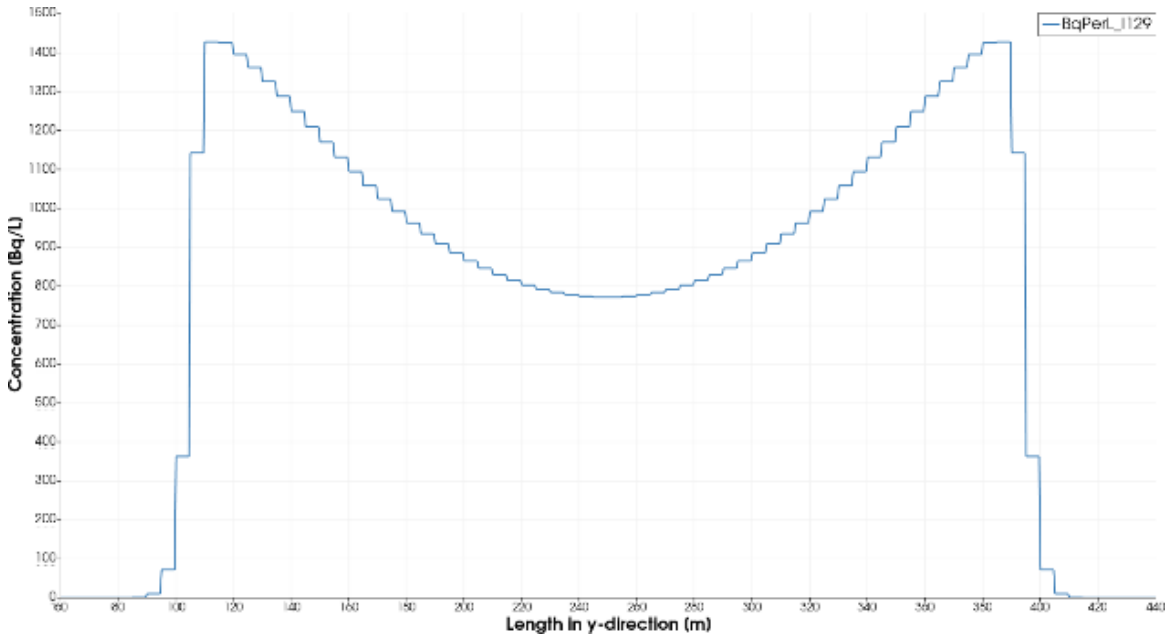

Figure 4.9.: Concentration over the cross section in y-direction of the aquifer at x =950 m, z = 10 m and t = 1.2e 8s

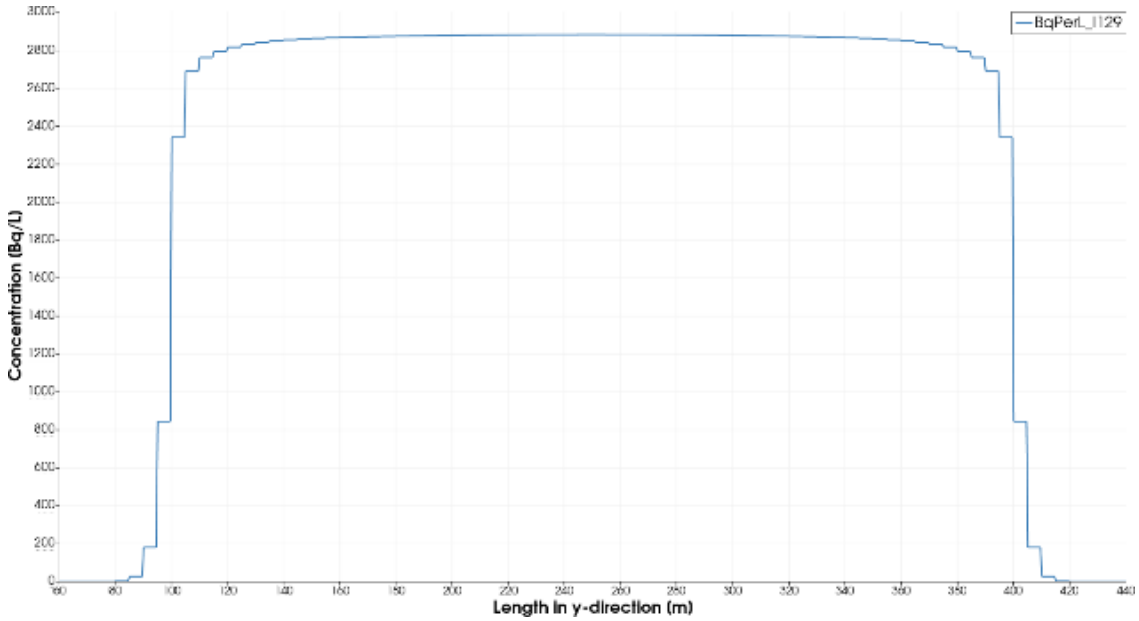

Figure 4.10.: Concentration over the cross section in y-direction of the aquifer at x =950 m, z = 10 m and t = 2.4e8 s

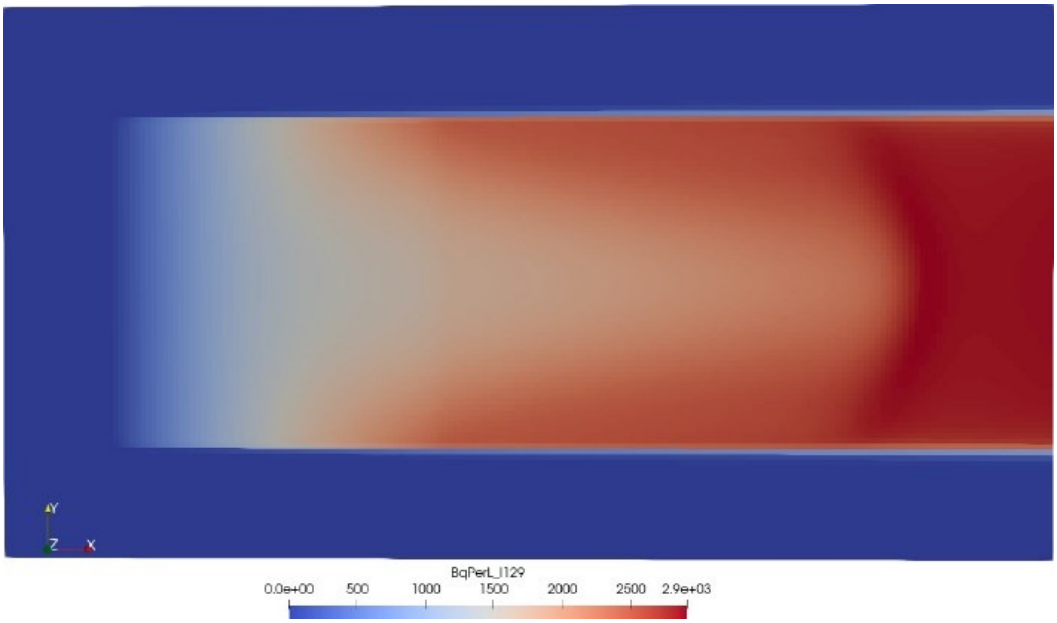

Figure 4.11.: Concentration plume at z = 10 m and t = 2.4e8 s

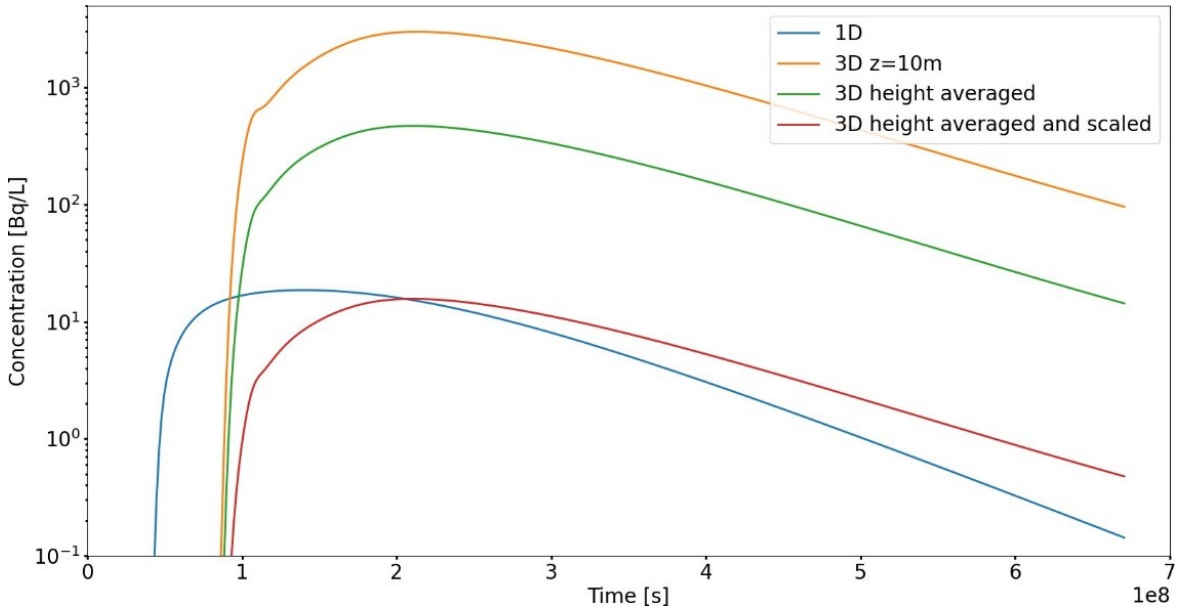

Figure 4.12.: Concentration over time for 1D (blue curve) and 3D (other curves) at x = 950 m and y = 250 m. The yellow curve depicts concentration valuesat the top of the aquifer z = 10 m, the green one the averaged value over the height of the aquifer, and the red one the average multiplied with theratio of the dilution factors between 1D and 3D.

In order to compare the results from the 3D simulations with the corresponding 1D results, we focus on the vertical line through the aquifer from z = 0 to 10 m at x = 950 mand y = 250 m. The temporal evolution of the concentration is shown in Fig. 4.12. Three different curves are depicted for the 3D case. The topmost curve corresponds tothe concentration at the top of the aquifer z = 10 m. Since the concentration decreases rapidly towards the bottom of the aquifer, the average over the height depicted in the middle curve is considerably smaller. For better comparability, the 3D result is further scaled with the ratio of the dilution factors between 1D and 3D. With the prescribed vertical flux of v_z = 3e-8 m/s and horizontal flux of v_x = 1.65e-5 m/s, the dilution factor in 1D is given as $v_z/v_x \approx$ 1.8e-3, implicitly assuming an extension of 1 m in vertical and horizontal direction. In 3D, the vertical flux acts over the 300 m horizontal extension of the landfill, while the horizontal flux acts over the 10 m aquifer height, yielding a 30 times higher dilution factor. Scaling the 3D result by the respective factor of 1/30 yields the lowest 3D curve in Fig. 4.12. While the peak concentration values are now very similar, the curves differ in

the arrival time of the radionuclideand the corresponding slopes before and after the peak values. The slower ramp-up time in the 3D curve until reaching the peak value and also the slower levelling off(or tailing) afterwards are due to the 300 m long infiltration distance underneath the landfill body.

To summarize, the 3D simulation results reveal some features and complexity which are obviously not represented in simplified 1D setups. However, the good qualitative agreement between the two scenarios shows that a 1D assumptions can be justified dependent on the questions posed. For realistic scenarios, also for the communicationto the public, we expect that the 3D scenarios are the appropriate choice, while the details of geometries, boundary conditions, etc. along with the respective features, for example, as we have seen in concentration plots above, need to be studied in detail. In particular at the science-policy interface, the communication of numerical simulation results is challenging in various aspects and requires good strategies with comprehensive assumptions and realistic results (Scheer, et al., 2020).

4.4 The Influence of the Choice of Boundary Conditions at the Top of the Model Domain

One aim of this project was the investigation of the influence of possible climate-related effects on the transport of the contaminants. We assume for this study that the effects of precipitation events, like rain of different intensity and frequency, as well as periods of drying out and strong evaporation, can be represented by the choice of boundary conditions at the top of the model domain. Effects of climate change on precipitation, temperature, or solar radiation are intensively under research and predicted described by the German Weather Service (DWD) (Deutscher Wetter Dienst). According to DWD reports, the climate in central Europe and Germany changes towards even higher temperatures in the summer while a similar mean precipitation rate is expected. However, the time between rain events may be increasing, resulting in more heavy rain events(Sec. 4.4.1), while increased evaporation due to higher temperatures and solar radiation my occur between rain periods (Sec. 4.4.2). Important to mention is that heavy rain events introduce a higher surface runoff (Sec. 4.4.3), which essentially needs to be considered by appropriate hydrological models. In this whole section the modelled radionuclide is ^{129}I.

4.4.1 Rain Events

Conceptual assumptions Let us keep the assumption that the mean precipitation during a modelled time period remains constant. For a principle study on the influence of different rain intensity and, accordingly, rain-event frequency, we decided to vary the length of time intervals between rain events and to scale the precipitation of the events, i.e., the flux rates, to the time between them. In order to keep things simple and comprehensive, we chose one day for the duration of a single rain event, corresponding to the commonly found information related to precipitation events in the field of hydrology (Maniak, 2016). An assumed choice of zero days between precipitation events results in the constant 0.8 m/y = 2.54e-5 kg/m^{2}s as mentioned above in Sec. 4.1, but without a sinusoidal profile in this case. Since the time scale of rain events is, thus, in days, we chose the time scale between events also in days. Consequently, the applied scaling of the precipitation rate of the specific rain event then looks like this:

$$\mathrm{m_{RainEvent}} = 2.54\mathrm{e}-5\,\frac{\mathrm{kg}}{\mathrm{m^2\ s\ d}}\cdot(1\ +\ \mathrm{d_{betweenEvents}}). \tag{33}$$

Exemplary results According to the suggested scaling, we varied the times between rain events and pictured the results of water saturation values at the top of the landfill in Fig. 4.13. The obvious result is the different amplitudes of the saturation peaks due to the different forced infiltration rates. Correspondingly, if we compare the profile of the saturation over the height of the landfill, as shown in Fig. 4.14, significant differences between the curves are visible. However, as will be shown below, this does not affect the radionuclide transport in the aquifer in the same clear way.

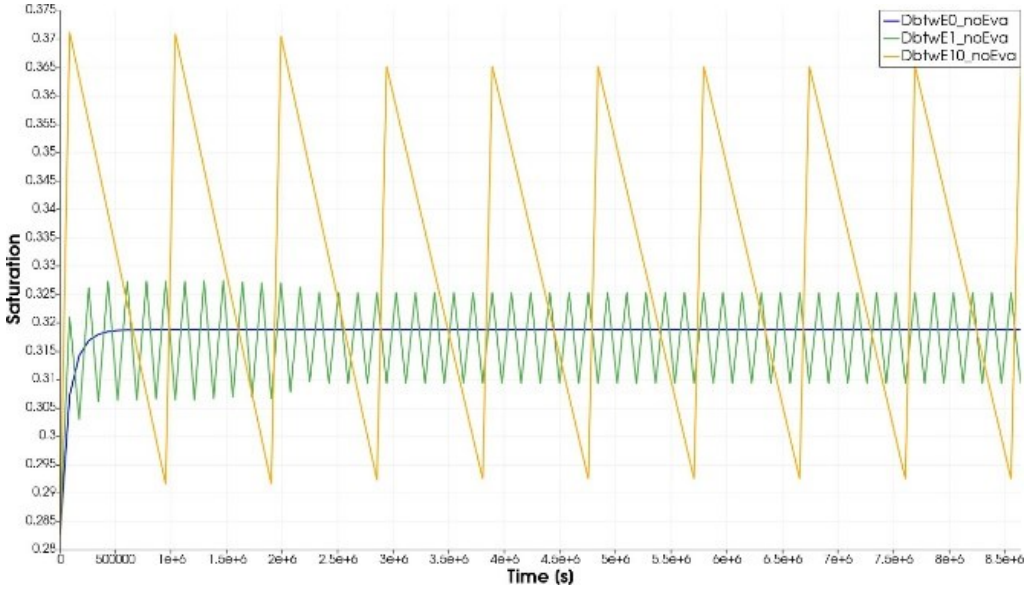

Figure 4.13.: Saturation over the time of the vadose zone and landfill for different days between rain events.

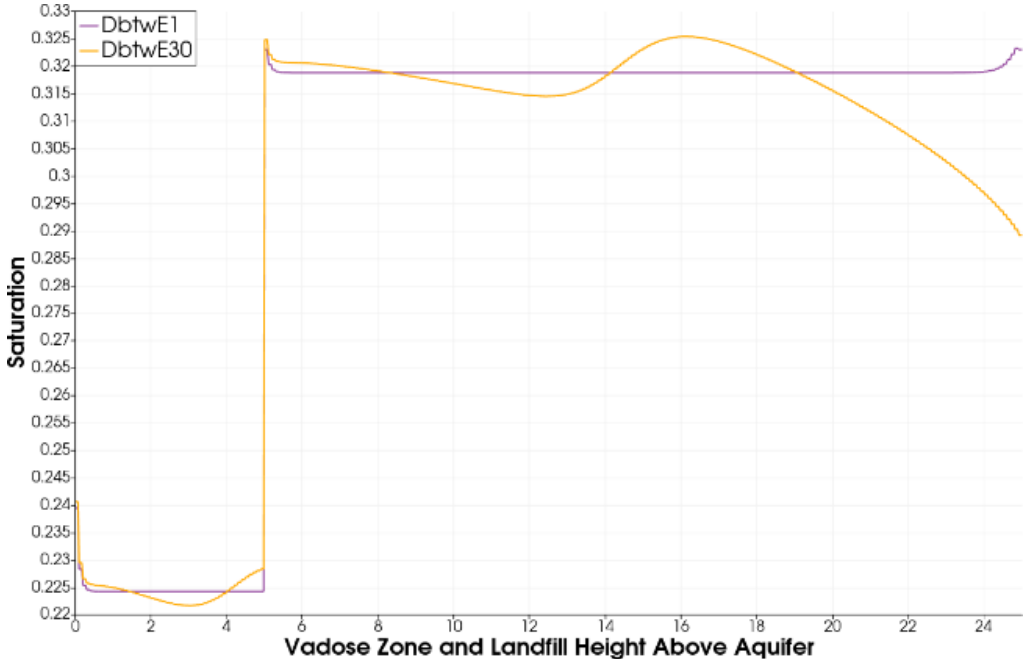

Figure 4.14.: Saturation over the height of the vadose zone and landfill for different days between rain events.

Plots of contamination curves over time for different choices of rain-event characteristics are shown in Fig. 4.15. In the same plot, there are curves where evaporationis considered (determined as discussed further below) and curves without evaporation considered. Although there is no significant deviation between all the curves, it can be seen in the details that the simulations with more time between rain events havea steeper gradient for the arrival of the contamination at the well. The landfill body effectively acts as a buffer with the chosen intervals between rain events not affecting the mean release rate of radionuclides into the aquifer significantly. The difference between the curves of different choices in rain-event characteristics becomes more distinct when evaporation is modelled during longer time periods of zero precipitation and when surface runoff is considered, see below.

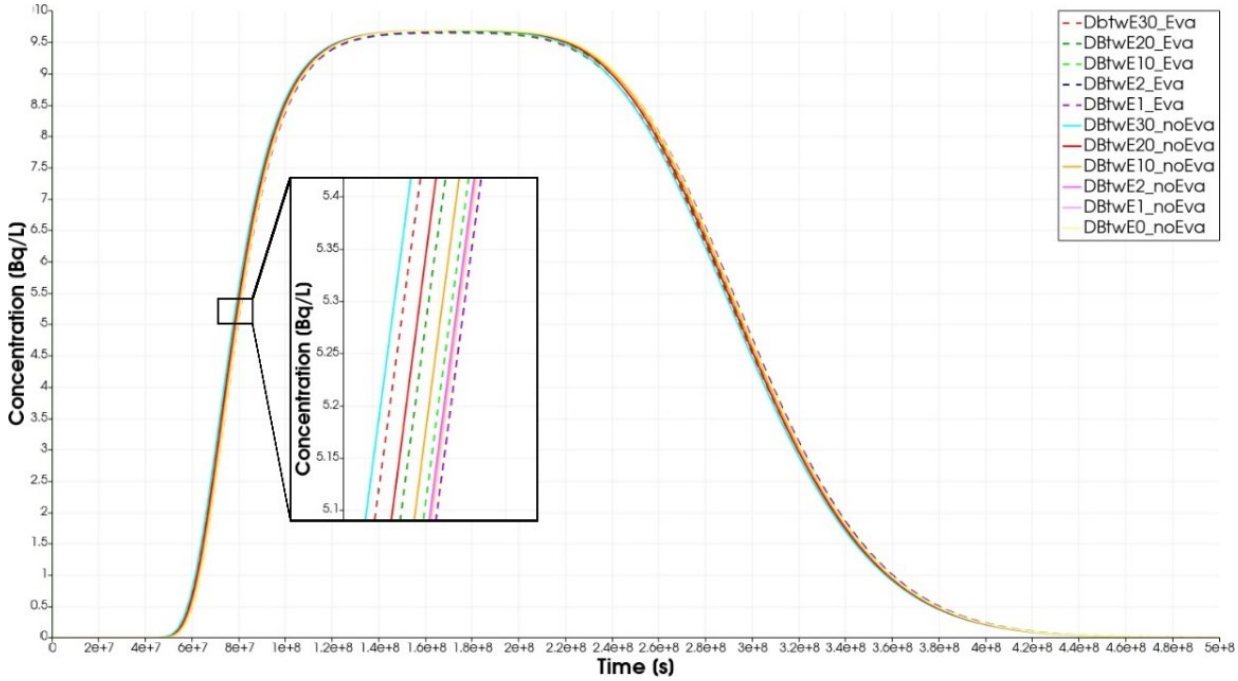

Figure 4.15.: Concentration over time for different rain-event characteristics and with-/without evaporation for ^{129}I, DbtwE refers here to Days between (rain) Events.

4.4.2 Evaporation

Evaporation was already included and briefly discussed in the results on the influence of rain events. For calculating the rate evaporation, we also need to make some conceptual assumptions. One of the possibilities is to use a non-isothermal multiphase multicomponent model, as it is available in DuMu^x and to calculate effective water-loss rates at the top boundary under given temperature conditions and the influence of solar radiation. However, the complexity of this 2p2cni model(2-phase-2-components-nonisothermal) is not sufficient to model all relevant effects of coupled heat and mass exchange at the interface between a porous medium and atmosphere, not to forget the influence of wind speed and air humidity, etc.; thus, to some extent empirical relations are required as explained below. Evaporation mass fluxes can then be estimated (model referred to as 2p2cevaporation) and inserted as boundary source terms in the previously discussed 2p or Richards-/Tracer models, while the heat exchange would be not further considered, since we do not solve an energy balance equation. For estimating the evaporation fluxes we chose to test two different models following the studies of (Heck, et al., 2020), (Heck, 2020), (Koch, et al., 2018) and (Nissler, et al., 2023).

Boundary layer model Following (Jambhekar, et al., 2015) or also described in (Koch, et al., 2018) evaporation from porous media is not only the phase change of liquid water to vapor at the top surface, but it includes the transport of liquid water from deeper regions. Accordingly, evaporation from porous media is conceptually divided into two stages. Briefly explained, stage I is characterized by a nearly constant evaporation rate as long as sufficient water is present to evaporate from the top surface. The evaporation during this stage is governed by the boundary layer thickness δ_{BL} and the water vapor pressure. At some point, the top surface is completely dry and the drying front moves into the soil body. This is the beginning of stage II evaporation, which is limited by diffusion. For simplicity, we assume for the implementations in the present study that the water saturation never drops low enough, which means it is about stage I evaporation and, thus, affected by the boundary layer thickness.
At the interface between the turbulent free flow of wind in the atmosphere and the porous medium of the soil, the beforehand mentioned boundary layer is formed. We may assume that the transport of water across this boundary layer is dominated by diffusion of water as vapor (Haghighi, et al., 2013). Additionally, we may assume that heat transfer is mainly governed by heat conduction (Fetzer, et al., 2016). With these assumptions, the mass flux of water vapor across the interface into the atmosphere can be calculated as (Fetzer, et al., 2016):

$$f^w = D_g^w \rho_g \frac{X_g^{w,BL} - X_g^{w,IF}}{\delta^{BL}}, \tag{34}$$

with the binary diffusion coefficient of water in the gas phase D^w, the mass fraction of water vapor in the gas phase in the boundary layer $X^{w,BL}{}_g$ and at the interface $X^{w,IF}{}_g$. The thickness of the boundary layer, δ_{BL}, is calculated for a turbulent free flow according to empirical approaches by (Fetzer, 2018):

$$\delta_{BL} = \frac{0.16x}{Re_x^{1/7}}, \tag{35}$$

with x as the point at which the boundary layer is developing. Here, we select 150 m as mean distance, because it represents half of the size of the landfill. The Reynolds number is also calculated with the same distance as characteristic length and an average wind speed of v_{wind} = 4 m/s. Furthermore, we assume a constant temperature of 30°C. With Eq. (34), we calculate a water flux of $f^w{}_{eva}$= 1.1061e-7 kg/m^{2}s leaving the modelled porous-medium system. Consequently, this value is applied as a prescribed boundary flux in the Richards-model on top of the landfill. We further assume that in periods, when there is no rain event, we automatically have the full evaporation flux. Of course, this assumption must be strongly questioned in reality. However, we feel it is consistent with the simplifications already made (e.g., we did not consider seasonal effects in the rain events either) and the aim of providing generic results to show a tendency dependent on the choice of the boundary, which have to be specified later on, for example, in extreme scenarios of climate change, etc.

Penman-Monteith model An alternative model to calculate the evaporation flux at the boundary is the Penman-Monteith equation, described for example in (Allen, et al., 1998), (Allen, et al., 2006), (Maniak, 2016), (Nissler, et al., 2023). It represents a hydrological approach describing an approximation to calculate a reference evapotranspiration ET index from given (measured) weather parameters. These parameters are usually measured on a 24 h basis. This approach takes further factors of influence into account as, for example, the surface type and its vegetation, which we assumed to be grass for simplicity and in order to be able to apply this approach exemplarily for the landfill scenario. Here, we adapt the notation of the model as introduced by (Nissler, et al., 2023), since it is consistent with the implementation in the DuMu^x model. The evapotranspiration rate ET is then calculated as:

$$ET = \frac{M_w}{\rho_w R T_{abs}} \frac{\kappa^2}{\ln\left(\frac{z_m - t_d}{z_0}\right)^2} u_m \cdot (e_{surf} - e_m), \tag{36}$$

with the universal gas constant R, the absolute temperature T in K, the von Karman constant κ, the height z, the velocity u and the vapor pressures e. m denotes here the point of the measurements in 2m height and surf the ones at the ground surface. Often in Eq. (36) the aerodynamic resistance r_a is used:

$$r_a = \frac{\ln\left(\frac{z_m - t_d}{z_0}\right)^2}{\kappa^2 u_m}, \tag{37}$$

which can be approximated by $208/v_m$ according to (Allen, et al., 1998). Due to a lack of specific data for the landfill water-pathway scenario, we decided to use data gathered from a separate project as reference (personal communication with colleagues in Stuttgart and published in (Nissler, et al., 2023)). The evaporation rates calculated in the model from the Nissler, et al. study on a daily basis over 15 months were averaged to obtain a mean rate of $f^w{}_{eva}$= 4.58e-5 kg/m^{2}s. In order to have the evaporative flux consistent with the precipitation rate, we calculated also an average precipitation rate from the Nissler, et al. data, which is in this particular case 7.63e-5 kg/m^{2}s. In their study, the evaporation rate accounts for around 60% of the precipitation; therefore, we also chose the same relation to be consistent. This results in a calculated evaporation flux of 2.5e-5 kg/m^{2}s · 60% = 1.5e-5 kg/m^{2}s. This was implemented as forced sink of water as boundary condition on the top of the landfill during no-rain periods.

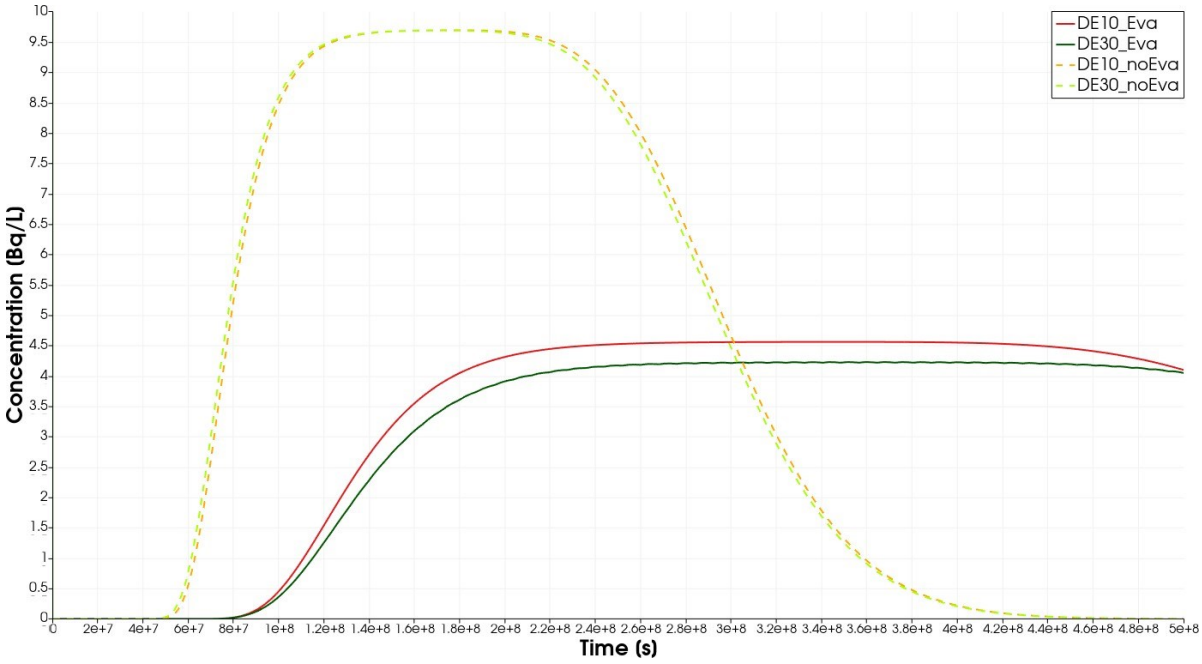

Figure 4.16.: Concentration of ^{129}I over time for different assumptions on the number of days between rain events and with evaporation calculated with Penman-Monteith approach and the observation point 500m from the landfill.

Effectively, as pictured in Fig. 4.16, with the above-mentioned assumptions with respect to the boundary conditions at the top, we have now a lower water inflow rate from the top boundary. The main reason is that the evaporation rate calculated by the more sophisticated (in terms of considered physics) Penman-Monteith model is in the order of a factor of 150 larger than the one calculated with the boundary layer modelin Sec. 4.4.2. Consequently, the propagating concentration front towards the well in 500 m distance from the landfill is significantly slower. With respect to the peak concentration, this value is also reduced since the contamination is more diluted in the aquifer, which is not assumed to be affected in its flow rate.

To summarize the insights from this intercomparison of approaches to consider evaporation, we can state that this is a major source of uncertainty with regard to assumptions taken in model approaches. The strong differences in the application of the two presented approaches are striking and underline the need to define realistic scenarios for specific risk assessments. The Penman-Monteith model requires more data, which is why it is difficult to use for generic studies, but it is reasonable to claim that it represents the more realistic approach to model evaporation.

Finally, we have to note that our presently applied model cannot distinguish between stage I and stage II evaporation. For that, we would need a non-isothermal multi-component model, which we certainly have available, but we deemed it appropriate and justified to save computational efforts and perform a simplified parameter study by only manipulating the effective boundary flux of water from the two models described above. We expect that a long dry period will reach a point where evaporative fluxes are limited by complete dry-out at the top and diffusion-limitation from deeper regions. This may slightly diminish the discrepancy between the different model approaches for long intervals between rain events. We further keep in mind, also for the following section, that - based on DWD-predicted climate scenarios - we assumed here a constant yearly precipitation rate, which is the reason for the observed changes in the comparison above, where the interval length between rain events has changed,which in turn changed precipitation intensity.

4.4.3 Surface Runoff

There is another effect, which is so far not considered when precipitation events of different intensity are evaluated. This is concerned with surface runoff, which is dependent on rain intensity and the

ability of the porous medium to take up water, thus models on the water content of the unsaturated porous medium.

A widely used model in hydrology for surface runoff is the curve number or SCS-method from the (formerly known as) US Soil Conservation Service (now: USDANatural Resources Conservation Service) (Maniak, 2016), (Slack, et al., 1980), (Soulis, 2021). This model introduces a runoff, which is subtracted from the precipitation or is used to calculate a runoff factor. The runoff is calculated after (Maniak, 2016) as:

$$Q = \frac{(N - I_a)^2}{N - I_a + S}, \qquad N > I_a, \tag{38}$$

with the runoff Q, the precipitation N and an initial loss I_a. It has to be noted, that the values here are in millimetres. Therefore, we have to convert the fluxes as implementedin the DuMu^x model from kg/m^{2}s to mm. With the information mentioned in Sec. 4.4.2, that in hydrology usually daily measurements are used, Eq. (38) misses the S, which we suggest to be calculated as:

$$S = \frac{1000}{CN} - 10, \tag{39}$$

with the values in inches. Converted to millimetres it requires to consider the factor 25.4:

$$S = \frac{25400}{CN} - 254, \qquad 0 < CN < 100. \tag{40}$$

The parameter CN stands for the maximum storage capacity of a soil and depends on parameters like the current water saturation, the soil usage, or the soil type. It is often used in agriculture, can be reliably determined by measurements, and can usually be found in tables for various soils. Considering examples as provided by (Maniak, 2016) a reasonable value for a landfill might be CN = 30. Results for different CN are shown in Fig. 4.17 and 4.18 for different choices of the assumed interval between rain events, i.e., 10 days and 30 days.

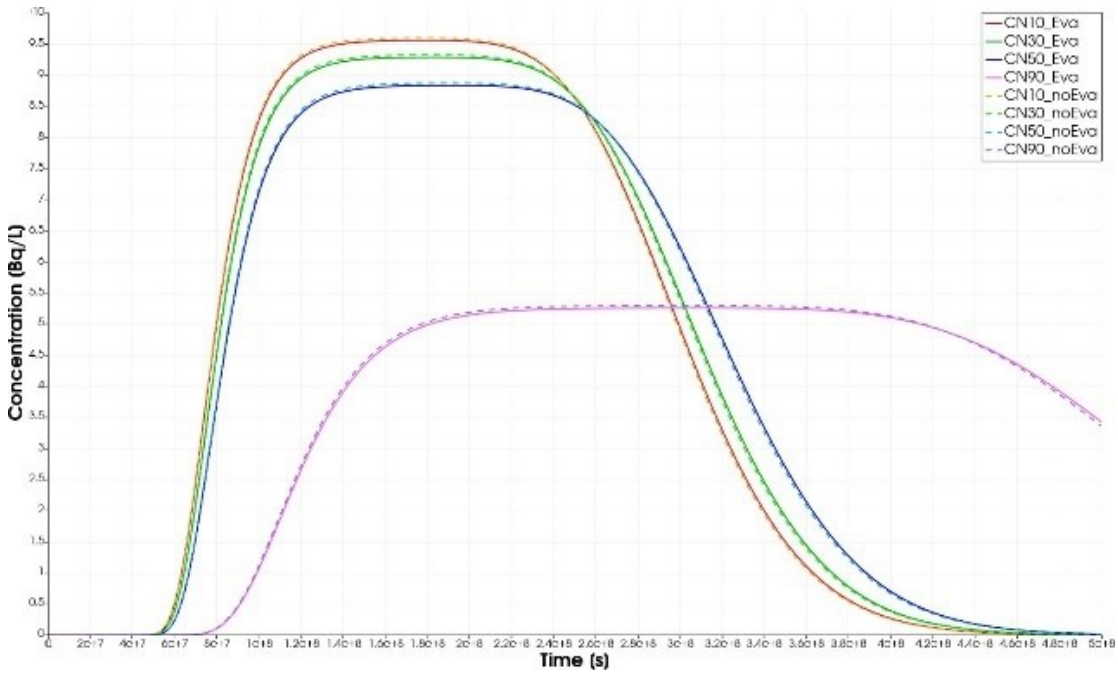

Figure 4.17.: Concentration of ^{129}I over time for different CN values for assumed intervals of 10 days between rain events with and with-out evaporation from the boundary layer evaporation model and surface runoff at the observation point 500m from the landfill

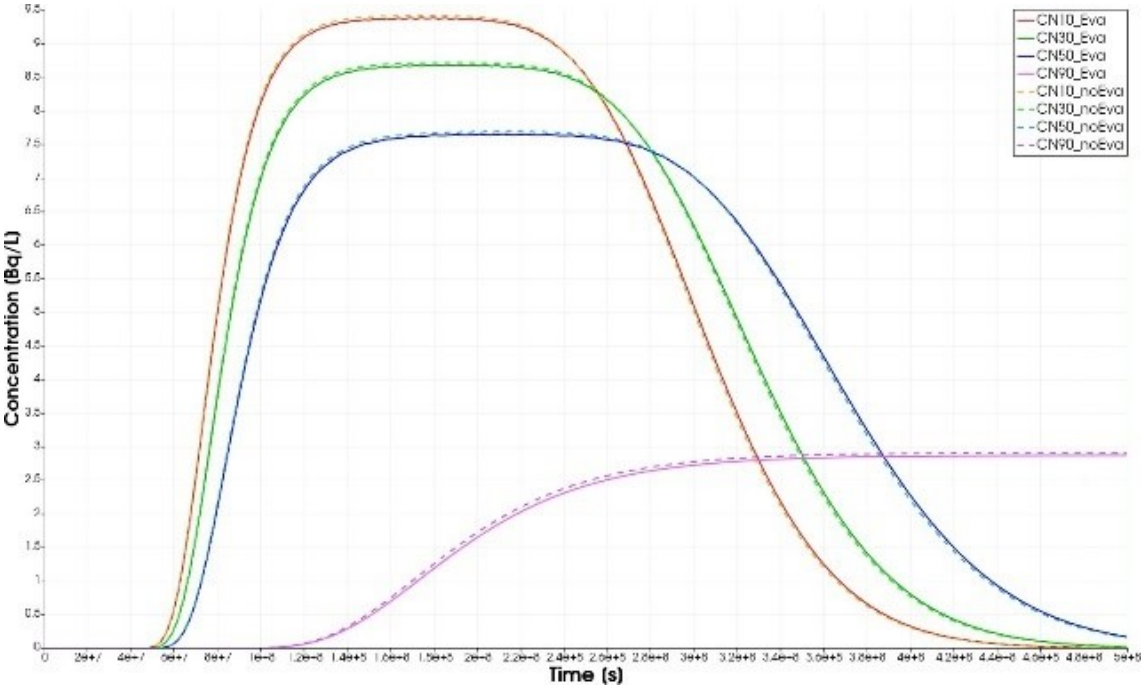

Figure 4.18.: Concentration of ^{129}I over time for different CN values for assumed intervals of 30 days (right) between rain events with and with-out evaporation from the boundary layer evaporation model and surface runoff at the observation point 500m from the landfill

From Eq. (38) and Eq. (39), we can derive that the runoff increases for high values of CN and high N. This is clearly visible in the concentration-over-time plots, both in Fig. 4.17 and in 4.18. In particular, the increased surface runoff for the 30 days intervals between rain events is interesting. We note again, that due to our assumption of constant yearly precipitation this implies stronger individual rain events, which is associated with a higher share of surface runoff. Thus, we have to conclude that surface runoff does significantly alter the effective share of precipitated water flowing through the landfill body, and it is necessary to take this into account for projected heavy rain events and climate-change scenarios.

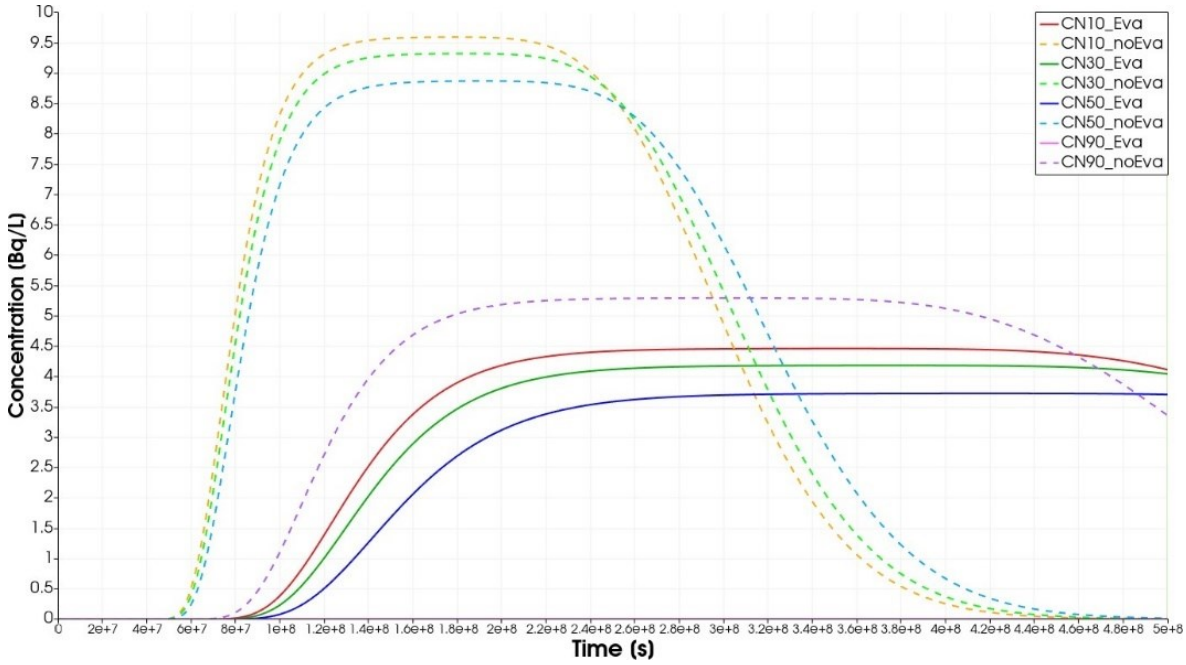

Figure 4.19.: Concentration of ^{129}I over time for different CN values, 10-day intervals between rain events, with and with-out evaporation calculated with the Penman-Monteith model and with surface runoff considered.

Finally, Fig. 4.19 provides an impression of the sensitivity of the concentration curve at the observation well with respect to the above-discussed hydrological effects. The plot underlines the strong effects of hydrological model assumptions on breakthrough concentrations in these generic scenarios. Again, to bring this into the context of the aims of this project, we need to emphasize that any preferential flow-path scenario, like in a macropore, may change the breakthrough curve. This has to be considered in specific scenario descriptions of geometric features and their properties and was, unfortunately beyond the scope of this project. Assuming that preferential flow, at least in the aquifer, is not dominant, we conclude that the expected conditions with progressing climate change, i.e. more rain events, longer hot dry periods, will lead to a reduced transport of radionuclides under the assumptions of a transport as solute. This may change, although not necessarily, under certain unfavourable conditions in colloidal transport through macropores. As elaborated in Chapter 1 of this report, we propose to invest here into joint experimental and numerical research work in the future.

5 Scientific summary and relation to IAEA Safety Report 44

The project has investigated different aspects of hydrodynamics and transport of radionuclides via the water pathway. This can be related to the IAEA Safety Report 44 (IAEA, 2005), specifically to Section 4.3.4, where the assumptions taken for the water pathway are elaborated. The SR 44 uses thoughtful analytical back-of-the-envelope calculations to assess potential impacts of radionuclides transported along the water pathway.

In his publication (Merk, 2012) from BfS has investigated how the calculations, basic assumptions and equations of the water-pathway scenario in SR 44 compare with the results from a process-based numerical simulation model that solves the partial differential equations of flow in unsaturated porous media, in this case the software package HYDRUS, which is well established and recognized in the scientific community. He elaborated on the influence of various model parameters in a numerical simulation study conducted in 1D. The Paper of Merk as the starting point of this project, has left open questions with regard to the influence of physical complexity that was not considered in the HYDRUS simulator and with regard to the influence of more than one spatial dimension in a landfill scenario or with regard to the influence of climate characteristics that alter, for example, rain intensity, precipitation frequency, or evaporation rates. The simulator DuMu^x, which was used as the working platform for this project, allows for a flexible implementation of conceptual modelling ideas and was used accordingly to implement and run comparative scenarios in order to assess the significance of the simplifying assumptions in SR 44 (IAEA, 2005) and (Merk, 2012).

Concerning hydrodynamics, we implemented and investigated model approaches to consider 'full' two-phase flow in unsaturated porous media in addition to the Richards model which assumes an infinitely mobile gas phase. Based on the results of this study, we feel it is safe to claim that the Richards equation is fairly accurate within the range of combinations of model parameters that can typically be expected for water-pathway scenarios consisting of a landfill and an aquifer. Deviations from this assessment may arise from particular settings of preferential pathways or other situations where a deviation from the Darcy regime, i.e., at higher Reynolds numbers, occurs. For that reason, we furthermore compared the Darcy model with an extended approach that allows for considering inertial effects (Forchheimer model). In this regard, we note that values for the Forchheimer coefficient, which are typically found in the literature, do not justify the application of the computationally much more expensive Forchheimer model. However, we point out that we have doubts regarding the limitation of Forchheimer coefficient's values to small numbers, see Sec. 2.1.2. It was shown, for example, in Fig. 2.8 that significantly higher values can lead to deviations in the results at higher Reynolds numbers. This might be the case for scenarios with macropores in the body of a landfill. Yet, it requires specific data to calibrate Forchheimer's coefficients.

Tracer transport for radionuclides considered as solutes that can decay, adsorb, desorb or be subject to dispersion was implemented and allows for the comparison of 1D and 3D scenarios, see Sec. 4. As expected, 3D models are computationally much more expensive, while they are no conservative choice in estimating the concentrations of radionuclides arriving at an assumed groundwater well downstream of a landfill. With respect to communication with the public or stakeholders, we consider them as appropriate due to the possibility of displaying model results in a realistic setting.

An issue that is still open after this project is the question of the influence of extreme preferential flow paths in landfills, where the assumptions of Darcy or Darcy-Forchheimer regimes are not valid anymore. They might develop as a worst-case scenario due to an extreme precipitation event that leads to flushing and mechanical abrasion in the landfill body, such that large open macropores may transport water, colloidal particles, and radionuclides. The implementation of such models is complex and requires a lot of additional mathematical abstractions of processes, which are not currently known to us to be available in the literature. Furthermore, a review of the literature on colloidal transport has shown that, in terms of mathematical models, there are typically relatively simple models employed to represent retardation, e.g. due to filtering, or sorption-like models (Langmuir, etc.). In any case, such processes would rather lead to colloidal transport being slower than solute transport. The possibility of colloidal transport being much faster than solute transport is also mentioned in the literature. This is the aspect which should

be given attention in future research. However, generic investigations may not be very purposeful in this regard, since the manifoldness of the unknowns in these processes seems to prohibit that. Therefore, we propose, as already indicated in the literature review, first chapter of this report, that joint numerical and experimental/site-specific investigations are required. Such research should already have answers to questions like: How exactly is the landfill constructed? What is the grain-size distribution of the bulk material? How homogeneous or heterogeneous is the landfill? Are there mineral liners underneath? As a lighthouse project or blueprint in that regard may serve the so-called FluidFlower initiative (Flemisch, et al., 2023), which was carried out in the context of geological storage of CO_2. The idea is to provide an experimental reference on a reasonable scale for modellers, who can test their ideas and approaches and validate their models without being speculative. We think that for a landfill/aquifer scenario with particular features of preferential flow this would be a good starting point for further research with regard to the still open questions.

Coming back to the IAEA SR 44, which refers to the choice of a realistic case and a low probable case with unfavourable conditions assumed for the latter, we are confident to claim that neither of the above-mentioned simplifications are more significant than (i) the actual choice in the assumptions of the scenario to be modelled and the choice of boundary conditions, see Sec. 4.4 of this report, and (ii) the possibilities of extreme scenarios leading to preferential flow. Thus, as a recommendation based on the resultsof this study, we propose to first of all carefully select the scenario, i.e., determining the initial and boundary conditions, identifying the driving forces (rain intensity, periodicity, etc.) for the water pathway, determining the model input parameters, most importantly the properties of the porous media with respect to transport (porosity, permeability, multiphase flow properties, dispersivity, and retardation properties, heterogeneities, potential preferential flow features). Upon that, we recommend that based on current knowledge both the SR 44 equations and the HYDRUS1D model used by (Merk, 2012) as well as our DuMu^x models are sufficiently accurate to predict the concentrations and arrival times of radionuclides in reliable orders of magnitude.

A major advantage of the DuMu^x tool we provide as a result from this project is its flexibility to address more complexity where desired. This allows for improving the process understanding where required and also for testing any kind of hypothesis on the sensitivity of parameters and processes.

The models and scenarios, which were used in this work, can be found in this public module: git.iws.uni-stuttgart.de/dumux-pub/winter2023a. Instructions on how to download and install it are found in a README file in this module, and for further questions on how to work with DuMu^x we refer to the website: dumux.org/.

6 Appendix

Table A.1.: Macropore parameters for the three implemented scenarios.

		Porosity [-]	x1 [m]	x2 [m]	y1 [m]	y2 [m]
Scenario (a)	Lens1	-	-	-	-	-
	Lens2	-	-	-	-	-
Scenario (b)	Lens1	0.94	3.0	3.2	0.0	10.0
	Lens2	0.94	7.2	7.6	0.0	10.0
Scenario (c)	Lens1	0.90	3.6	4.0	4.0	10.0
	Lens2	0.94	7.4	7.6	0.0	10.0

Table A.2.: Parameters for the Matern model in gstat.

Parameter	Value
v	2.5
r	2
sill	0.02
anisotropy angle	90
anisotropy factor	0.4

7 Literaturverzeichnis

[1] **Ahusborde, E., Amaziane, B. und Jurak, M. 2015.** 3D numerical simulation by upscaling of gas migration through engineered and geological barriers for a deep repository for radioactive waste. Geological Society, London, Special Publications. 2015, Bd. 415, S. 123 - 141.

[2] **Ahusborde, E., Kern, M. und Vostrikov, V. 2015.** Numerical simulation of two-phase multicomponent flow with reactive transport in porous media: application to geological sequestration of CO 2. ESAIM: Proc. 2015, Bd. 50, S. 21-39.

[3] **Allen, R. G. und Pereira, L. S. 1998.** Crop evapotranspiration guidelines for computing crop requirements. FAO Irrig. Drain. Report modeling and application. Journal of Hydrology. 1998, Bd. 285 S. 19-40.

[4] **Allen, R. G., et al. 2006.** A recommendation on standardized surface resistance for hourly calculation of reference ETo by the FAO56 Penman-Monteith method. Agricultural Water Management. 2006, Bd. 81 S. 1-22.

[5] **Amaziane, B., Ossmani, M. E. und Serres, C. 2008.** Numerical modeling of the flow and transport of radionuclides in heterogeneous porous media. Computational Geosciences. 2008, Bd. 12 S. 437-449.

[6] **Artmann, A., et al. 2014.** Abschlussbericht GRS - 342: Anwendung und Weiterentwicklung von Modellen für Endlagersicherheits- analysen auf die Freigabe radioaktiver Stoffe zur Deponierung. 2014. ISBN: 9783944161228.

[7] **Artmann, A., et al. 2020.** GRS-506 Freigabekonzepte einer neuen Strahlenschutzverordnung nach Euratom- Grundnormen 2013 in der Anwendung Freigabekonzepte. 2020. ISBN: 9783946607915.

[8] **Balhoff, M. T. und Wheeler, M. F. 2009.** A predictive pore-scale model for non-Darcy flow in porous media. SPE Journal. 2009, Bd. 14, S. 579–587.

[9] **Bastian, P., et al. 2008.** A generic grid interface for parallel and adaptive scientific computing. Part I: Abstract framework. Computing . July 2008, Bd. 82, S. 103-119.

[10] **Bastian, P., et al. 2008.** A generic grid interface for parallel and adaptive scientific computing. Part II: Implementation and tests in DUNE. Computing. July 2008, Bd. 82, S. 121-138.

[11] **Bastian, P., et al. 2021.** The DUNE framework: Basic concepts and recent developments. Computers and Mathematics with Applications. 2021, Bd. 81, S. 75-112.

[12] **Bear, J. 1972.** Dynamics of Fluids in Porous Media. Elsevier, 1972.

[13] **Bear, J. und Bachmat, Y. 1990.** Introduction to Modeling of Transport Phenomena in Porous Media. Kluwer Academic Publishers, 1990.

[14] **Bedrikovetsky, P., et al. 2011.** Modified Particle Detachment Model for Colloidal Transport in Porous Media. Transport in Porous Media. 2011, Bd. 86, S. 353-383.

[15] **Beven, K. und Germann, P. 1982.** Macropores and water flow in soils. Water Resources Research. 1982, Bd. 18, S. 1311–1325.

[16] **Bianchi, M., Liu, H. H. und Birkholzer, J. T. 2015.** Radionuclide transport behavior in a generic geological radioactive waste repository. Groundwater. 2015, Bd. 53, S. 440-451.

[17] **Brooks, A. N. und Corey, A. T. 1964.** Hydraulic Properties of Porous Media. Fort Collins, Colorado State University, 1964.

[18] **Buckingham, E. 1907.** Studies on the movement of soil moisture. USDA Bureau of Soils, Washington, 1907, Bulletin 38.

[19] **Chen, C. und Wagenet, R. J. 1992.** Simulation of water and chemicals in macropore soils Part 1. Representation of the equivalent macropore influence and its effect on soilwater flow. Journal of Hydrology. 1992, Bd. 130, S. 105–126.

[20] **Cheng, C. und Chen, X. 2007.** Evaluation of methods for determination of hydraulic properties in an aquifer-aquitard system hydrologically connected to a river. Hydrogeology Journal. 2007, Bd. 15, S. 669–678.

[21] **Christiansen, J. S., et al. 2004.** Modelling of macropore flow and transport processes at catchment scale. Journal of Hydrology. 2004, Bd. 299, S. 136–158.

[22] **Class, H., et al. 2021.** On the role of density-driven dissolution of CO2 in phreatic karst systems. Water Resources Research. 2021, Bd. 57, S. e2021WR030912.

[23] **Dalla Valle, N., et al. 2017.** Modeling macropore seepage fluxes from soil water content time series by inversion of a dual permeability model. Hydrology and Earth System Sciences Discussions. 2017, Preprint, S. 1–31.

[24] **Darcy, H. 1856.** Les fontaines de la ville de Dijon. Paris : Dalmont, 1856.

[25] **de Vries, J. J. und Simmers, I. 2002.** Groundwater recharge: An overview of process and challenges. Advances in Water Resources. 2002, Bd. 10, S. 5–17.

[26] **Deutscher Wetter Dienst.** Definition Starkregen. Definition Starkregen. Accessed: 2021-10-30. https://www.dwd.de/DE/service/lexikon/begriffe/S/Starkregen.html

[27] **Deutscher Wetter Dienst.** Klimawandel. Accessed: 2023-07-13. https://www.dwd.de/DE/klimaumwelt/klimawandel/klimawandel_node.html

[28] **Dumux Documentation.** Tracer Model Defintion. Accessed: 2022-03-28. https://dumux.org/docs/doxygen/master/a18456.html

[29] **Fetzer, T. 2018.** Coupled Free and Porous-Medium Flow Processes Affected by Turbulence and Roughness-Models, Concepts and Analysis. University of Stuttgart, 2018.

[30] **Fetzer, T., Smits, K. M. und Helmig, R. 2016.** Effect of Turbulence and Roughness on Coupled Porous-Medium/Free-Flow Exchange Processes. Transport in Porous Media. 2016, Bd. 114, S. 395-424.

[31] **Flemisch, B., et al. 2011.** DuMux: DUNE for multi-{phase,component,scale,physics,...} flow and transport in porous media. Advances in Water Resources. 2011, Bd. 34, 9, S. 1102-1112.

[32] **Flemisch, B., et al. 2023.** The FluidFlower international benchmark study: Process, modelling results, and comparison to experimental data. Transport in Porous Media. 2023, Bd. /s11242-023-01977-7.

[33] **Fourar, M. und Lenormand, R. 2000.** Inertial Effects in Two-Phase Flow through Fractures. Oil and Gas Science and Technology. 2000, Bd. 55, S. 259–268.

[34] **Fourar, M., et al. 2005.** Inertia effects in high-rate flow through heterogeneous porous media. Transport in Porous Media. 2005, Bd. 60, S. 353–370.

[35] **Frimmel, F. H., von der Kammer, F. und Flemming, H.-C. 2007.** Colloidal transport in porous media. Springer, 2007. S. 291. ISBN: 9783540713388.

[36] **Gerke, H. H. und van Genuchten, M. T. 1993.** A dual-porosity model for simulating the preferential movement of water and solutes in structured porous media. Water Resources Research. 1993, Bd. 29, S. 305–319.

[37] **Gläser, D., et al. 2017.** A discrete fracture model for two-phase flow in fractured porous media. Advances in Water Resources. 2017, Bd. 110, S. 335-348.

[38] **Hagemann, B., et al. 2016.** Hydrogenization of underground storage of natural gas: Impact of hydrogen on the hydrodynamic and bio-chemical behavior. Computational Geosciences. 2016, Bd. 20, S. 595-606.

[39] **Haghighi, E., et al. 2013.** Evaporation rates across a convective air boundary layer are dominated by diffusion. Water Resources Research. 2013, Bd. 49, S. 1602-1610.

[40] **Harr, J. L. 2007.** Precise Calculation Of Complex Radioactive Decay Chains. Graduate School of Engineering and Management. Graduate School of Engineering and Management, AFIT, 2007. S. 92, Master Thesis.

[41] **Haskard, K. A. 2007.** An anisotropic Matérn spatial covariance model : REML estimation and properties. University of Adelaide, 2007.

[42] **Heck, K. 2020.** Modelling and analysis of multicomponent transport at the interface between free-and porous-medium flow-influenced by radiation and roughness. University of Stuttgart, 2020.

[43] **Heck, K., et al. 2020.** Influence of Radiation on Evaporation Rates: A Numerical Analysis. Water Resources Research. 2020, Bd. 56, DOI: 10.1029/2020WR027332.

[44] **Helmig, R. 1997.** Multiphase Flow and Transport Processes in the Subsurface - A Contribution to the Modeling of Hydrosystems. Springer Verlag, 1997.

[45] **Helmig, R., et al. 2013.** Model coupling for multiphase flow in porous media. Advances in Water Resources. 2013, Bd. 51, S. 52-66.

[46] **Hommel, J. und Coltman, E. Class, H. 2018.** Porosity–Permeability Relations for Evolving Pore Space: A Review with a Focus on (Bio-)geochemically Altered Porous Media. Transport in Porous Media. 2018, Bd. 124, S. 589–629.

[47] **HZDR und GRS. 2018.** GRS-500: Smart Kd -Concept for Long-term Safety Assessments-Extension towards more Complex Applications. Gesellschaft für Anlagen- und Reaktorsicherheit (GRS) gGmbH. 2018. S. 365, Tech. rep. ISBN: 9783946607854.

[48] **IAEA. 2004.** Application of the concepts of exclusion, exemption and clearance (IAEA RS-G-1.7). International Atomic Energy Agency. 2004. S. 1–39, Tech. rep. ISBN: 9201094043 ISSN: 09208542 15730484.

[49] **IAEA. 2005.** SR 44: Derivation of Activity Concentration Values for Exclusion , Exemption and Clearance. International Atomic Energy Agency. 2005. S. 141, Tech. rep.

[50] **Ishaku, J. M., Gadzama, E. W. und Kaigama, U. 2011.** Evaluation of empirical formulae for the determination of hydraulic conductivity based on grain-size analysis. Journal of Geology and Mining Research. 2011, Bd. 3, S. 105–113.

[51] **Jambhekar, V. A., et al. 2015.** Free-Flow-Porous-Media Coupling for Evaporation-Driven Transport and Precipitation of Salt. Transport in Porous Media. 2015, Bd. 110, S. 251-280.

[52] **Keim, L. 2022.** Coupled flow, transport amd geochemical processes in karstic fractures. Institute for Modelling Hydraulic and Environmental Systems, University of Stuttgart. 2022. Master's Thesis.

[53] **Knapp, R. B., Chiarappa, M. L. und Durham, W. B. 2000.** An experimental exploration of the transport and capture of abiotic colloids in a single fracture. Water Resources Research. 2000, Bd. 36, S. 3139-3149.

[54] **Koch, T., et al. 2018.** A New Simulation Framework for Soil-Root Interaction, Evaporation, Root Growth, and Solute Transport. Vadose Zone Journal. 2018, Bd. 17, S. 1-21.

[55] **Koch, T., et al. 2021.** DuMux 3 – an open-source simulator for solving flow and transport problems in porous media with a focus on model coupling. Computers and Mathematics with Applications. 2021, Bd. 81, S. 423-443.

[56] **Kodešova, R., Kozak, J. und Šimůnek, J. 2006.** Numerical Study of Macropore Impact on Ponded Infiltration in Clay Soils. Soil and Water Research. 2006, Bd. 1, S. 16–22.

[57] **Kumar, M. Ranjit, Meenambal, T. und Kumar, V. 2017.** Macropore flow as a groundwater component in hydrologic simulation: Modelling, applications and results. Current Science. 2017, Bd. 112, S. 1197–1207.

[58] **Leverett, M.C. 1941.** Capillary behaviour in porous. solids. Trans. Am. Inst. Min. Metall. 1941, Bd. 142, S. 152-169.

[59] **Ma, H. und Ruth, D. W. 1993.** The microscopic analysis of high Forchheimer number flow in porous media. Transport in Porous Media. 1993, Bd. 13, S. 139–160.

[60] **Macini, P., Mesini, E. und Viola, R. 2011.** Laboratory measurements of non-Darcy flow coefficients in natural and artificial unconsolidated porous media. Journal of Petroleum Science and Engineering. 2011, Bd. 77, S. 365–374.

[61] **Malkovsky, V. I. und Pek, A. A. 2009.** Effects of Colloids on Transfer of Radionuclides by Subsurface Water. Geology of Ore Deposits. 2009, Bd. 5, S. 79-92.

[62] **Maniak, U. 2016.** Hydrologie und Wasserwirtschaft. Springer Berlin Heidelberg, 2016.

[63] **McCarthy, J. F. und Zachara, J. M. 1989.** Subsurface transport of contaminants. Environmental Sciences & Technology. 1989, Bd. 23, S. 496-502.

[64] **Merk, R. 2012.** Numerical modeling of the radionuclide water pathway with HYDRUS and comparison with the IAEA model of SR 44. Journal of Environmental Radioactivity. 2012, Bd. 105, S. 60–69.

[65] **Minasny, B. und McBratney, A. B. 2005.** The Matérn function as a general model for soil variograms. Geoderma. 2005, Bd. 128, S. 192–207.

[66] **Moridis, G. J., et al. 2001.** Preliminary 3-D site-scale studies of radioactive colloid transport in the unsaturated zone at Yucca Mountain, Nevada. Earth Sciences Division, Lawrence Berkeley National Laboratory. Earth Sciences Division, Lawrence Berkeley National Laboratory, LBNL-45876, 2001. Tech. rep.

[67] **Müller, H. S., Herold, G. und Fleischer, K. 2007.** Rückbau kerntechnischer Anlagen - Eindringen von Radionukliden in Betonoberflächen und Freisetzung eingedrungender Aktivität aus Bauschutt und Beton. Univ., Inst. f. Massivbau u. Baustofftechnologie. Karlsruhe, 2007. S. 197, Tech. rep.

[68] **Nagasaki, S. und Nakayama, S. 2015.** Radioactive Waste Engineering and Management. ACNE. Springer, 2015.

[69] **National Research Council. 2001.** Conceptual Models of Flow and Transport in the Fractured Vadose Zone. The National Academies Press, 2001. ISBN: 9780309073028.

[70] **Nayagum, D., Schäfer, G. und Mosé, R. 2004.** Modelling Two-Phase Incompressible Flow in Porous Media Using Mixed Hybrid and Discontinuous Finite Elements. Computational Geosciences. 2004, Bd. 8, S. 49-73.

[71] **Nield, D. A. und Bejan, A. 2008.** Convection in porous media. Springer, Cham, 2008. S. 1–45. Bd. 165. ISBN: 9783319495613 ISSN: 2196968X.

[72] **Nissler, E., et al. 2023.** Heat Transport from Atmosphere Through the Subsurface to Drinking Water Supply Pipes. Vadose Zone Journal. 2023. DOI:10.1002/vzj2.20286.

[73] **Nordbotten, J. M., et al. 2012.** Uncertainties in practical simulation of CO2 storage. International Journal of Greenhouse Gas Control. 2012, Bd. 9, S. 234-242.

[74] **Novak, M., et al. 2014.** Conditional clearance of radioactive demolition waste in motorway scenario. Nuclear Science and Technology. 2014, Bd. 4, S. 854-857.

[75] **Nuske, K. 2014.** Beyond Local Equilibrium — Relaxing local equilibrium assumptions in multiphase flow in porous media. University of Stuttgart, 2014. ISBN: 9783942036412.

[76] **Odong, J. 2007.** Evaluation of Empirical Formulae for Determination of Hydraulic Conductivity based on Grain-Size Analysis. Journal of American Science. 2007, Bd. 3, S. 54-60.

[77] **Otto, S. A.** How to normalize the RMSE [Blog post]. Accessed: 13-10-2021. https://www.marinedatascience.co/blog/2019/01/07/normalizing-the-rmse/.

[78] **Pebesma, E. J. und Graeler, B. 2020.** R-Package ‘gstat' : Spatial and Spatio-Temporal Geostatistical Modelling, Prediction and Simulation Description. 2020.

[79] **R Core-Team. 2018.** R: A Language and Environment for Statistical Computing. R Foundation for Statistical Computing, 2018.

[80] **Richards, L. A. 1931.** Capillary conduction of liquids through porous mediums. Cornell University, 1931.

[81] **Rybak, I. 2016.** Mathematical modeling of coupled free flow and porous medium systems. Universität Stuttgart: SRC SimTech, 2016.

[82] **Saadatpoor, E., Bryant, S. L. und Sepehrnoori, K. 2009.** Effect of capillary heterogeneity on buoyant plumes: A new local trapping mechanism. Energy Procedia. 2009, Bd. 1, S. 3299–3306.

[83] **Scheer, D., Class, H. und Flemisch, B. 2020.** Subsurface Environmental Modelling Between Science and Policy. Springer, 2020.

[84] **Scheidegger, A. E. 1961.** General Theory of Dispersion in Porous Media. Journal of Geophysical Research. 1961, Bd. 66, S. 3273-3278.

[85] **Schwenck, N., et al. 2015.** Dimensionally reduced flow models in fractured porous media: crossings and boundaries. Computational Geosciences. 2015, Bd. 19, S. 1219-1230.

[86] **Seher, H., et al. 2016.** Modelling contaminant transport in generic landfills for decommissioning waste from German nuclear power plants. Progress in Nuclear Energy. 2016, Bd. 89, S. 46–56.

[87] **Sezer, A., Göktepe, A. B. und Altun, S. 2009.** Estimation of the permeability of granular soils using neuro-fuzzy system. CEUR Workshop Proceedings. 2009, Bd. 475, S. 333–342.

[88] **Shi, W., et al. 2018.** Numerical modeling of non-Darcy flow behavior of groundwater outburst through fault using the Forchheimer equation. Journal of Hydrologic Engineering. 2018, Bd. 23, S. 04017062.

[89] **Šimůnek, J., et al. 2003.** Review and comparison of models for describing non-equilibrium and preferential flow and transport in the vadose zone. Journal of Hydrology. 2003, Bd. 272, S. 14–35.

[90] **Šimůnek, J., Van Genuchten, M. Th und Šejna, M. 2016.** Recent developments and applications of the HYDRUS computer software packages. Vadose Zone Journal. 2016, Bd. 15, S.1-25.

[91] **Slack, R. B. und Welch, R. 1980.** SOIL CONSERVATION SERVICE RUNOFF CURVE NUMBER ESTIMATES FROM LANDSAT DATA. JAWRA Journal of the American Water Resources Association. 1980, Bd. 16, S. 887-893.

[92] **Sobieski, W. und Trykozko, A. 2011.** Sensitivity Aspects of Forchheimer's Approximation. Transport in Porous Media. 2011, Bd. 89, S. 155–164.

[93] **Soulis, K. X. 2021.** Soil conservation service curve number (SCS-CN) method: Current applications, remaining challenges, and future perspectives. Water. January 2021, Bd. 13. https://doi.org/10.3390/w13020192.

[94] **Stadler, L., Hinkelmann, R. und Helmig, R. 2012.** Modeling Macroporous Soils with a Two-Phase Dual-Permeability Model. Transport in Porous Media. 2012, Bd. 95, S. 585–601.

[95] **Steefel, C. I., et al. 2015.** Reactive transport codes for subsurface environmental simulation. Computational Geosciences. 2015, Bd. 19, S. 445–478.

[96] **Stockmann, M., et al. 2017.** Smart Kd-values, their uncertainties and sensitivities - Applying a new approach for realistic distribution coefficients in geochemical modeling of complex systems. Chemosphere. 2017, Bd. 187, S. 277–285.

[97] **Sukop, M. C., et al. 2013.** Evaluation of permeability and non-Darcy flow in vuggy macroporous limestone aquifer samples with lattice Boltzmann methods. Water Resources Research. 2013, Bd. 49, S. 216–230.

[98] **Takhanov, D. 2011.** Forchheimer Model for Non-Darcy Flow in Porous Media and Fractures. Imperial College London, 2011.

[99] **Tecklenburg, J., et al. 2016.** Multi-rate mass transfer modeling of two-phase flow in highly heterogeneous fractured and porous media. Advances in Water Resources. 2016, Bd. 91, S. 63-77.

[100] **Thauvin, F. und Mohanty, K. K. 1998.** Network Modeling of Non-Darcy Flow Through Porous Media. Transport in Porous Media. 1998, Bd. 31, S. 19–37.

[101] **U.S. Environmental Protection Agency. 1999.** Understanding variation in partition coeffcient, Kd, values. Volume II: Review of Geochemistry and Available Kd Values for Cadmium, Cesium, Chromium, Lead, Plutonium, Radon, Strontium, Thorium, Tritium (3 H), and Uranium. 1999.

[102] **U.S. Environmental Protection Agency. 1999.** Understanding variation in partition coefficient, Kd, values. Volume I: The Kd Model, Methods of Measurement, and Application of Chemical Reaction Codes. 1999.

[103] **U.S. Environmental Protection Agency. 1999.** Understanding Variation in Partition Coefficient, Kd, values. Volume III: Review of Geochemistry and Available Kd Values for Americium, Arsenic, Curium, Iodine, Neptunium, Radium, and Technetium. 1999.

[104] **Van Genuchten, M. Th. 1980.** A closed-form equation for predicting the hydraulic conductivity of unsaturated soils. Soil Sci. Soc. Am. J. 1980, Bd. 44, S. 892-898.

[105] **Walter, L., et al. 2012.** Brine migration resulting from CO2 injection into saline aquifers - An approach to risk estimation including various levels of uncertainty. International Journal of Greenhouse Gas Control. 2012, Bd. 9, S. 495-506.

[106] **Wang, L., et al. 2019.** Experimental investigation of flow characteristics in porous media at low Reynolds numbers (Re → 0) under different constant hydraulic heads. Water. 2019, Bd. 11. https://doi.org/10.3390/w11112317.

[107] **Weishaupt, K., et al. 2016.** Numerical Investigation on the Benefits of Preheating for an Increased Thermal Radius of Influence During Steam Injection in Saturated Soil. Transport in Porous Media. September 2016, Bd. 114, 2, S. 601-621.

[108] **Winter, R., et al. 2022.** A Study on Darcy versus Forchheimer Models for Flow through Heterogeneous Landfills including Macropores. Water. 2022, Bd. 14. https://doi.org/10.3390/w14040546

[109] **Wu, Y. 2002.** Numerical Simulation of Single-Phase and Multiphase Non-Darcy Flow in Porous and Fractured Reservoirs. Transport in Porous Media. 2002, Bd. 49, S. 209–240.

[110] **Wu, Y. S., et al. 2011.** Analysis of Multiphase Non-Darcy Flow in Porous Media. Transport in Porous Media. 2011, Bd. 88, S. 205–223.

[111] **Zeng, Z. und Grigg, R. 2006.** A Criterion for Non-Darcy Flow in Porous Media. Transport in Porous Media. 2006, Bd. 63, S. 57–69.

[112] **Zhang, A. 2013.** Numerical Investigation of multiphase Darcy-Forchheimer flow and contaminant transport during SO 2 co-injection with CO 2 in deep saline aquifers. Georgia Institute of Technology, 2013.

[113] **Zhang, J. und Xing, H. 2012.** Numerical modeling of non-Darcy flow in near-well region of a geothermal reservoir. Geothermics. 2012, Bd. 42, S. 78–86.

[114] **Zhang, S. 2015.** Relationship between Particle Size Distribution and Porosity in Dump Leaching. The University of British Columbia, 2015.